


Experimental Realization and Characterization of Stabilized Pair-Coherent States

Jeffrey M. Gertler,^{1,†} Sean van Geldern,^{1,†} Shruti Shirol,¹ Liang Jiang,² and Chen Wang^{1,*}

¹*Department of Physics, University of Massachusetts-Amherst, Amherst, Massachusetts 01003, USA*

²*Pritzker School of Molecular Engineering, University of Chicago, Chicago, Illinois 60637, USA*

 (Received 21 October 2022; revised 20 February 2023; accepted 22 March 2023; published 2 May 2023)

The pair-coherent state (PCS) is a theoretical extension of the Glauber coherent state to two harmonic oscillators. It is an interesting class of non-Gaussian continuous-variable entangled state and it is also at the heart of a promising quantum error-correction code: the pair-cat code. Here, we report an experimental demonstration of the pair-coherent state of microwave photons in two superconducting cavities. We implement a cross-cavity pair-photon driven-dissipation process, which conserves the photon-number difference between cavities and stabilizes the state to a specific complex amplitude. We further introduce a technique of quantum subspace tomography, which enables direct measurements of individual coherence elements of a high-dimensional quantum state without global tomographic reconstruction. We characterize our two-mode quantum state with up to four photons in each cavity using this subspace tomography together with direct measurements of the photon-number difference and the joint Wigner function. We identify the spurious cross-Kerr interaction between the cavities and our dissipative reservoir mode as a prominent dephasing channel that limits the steady-state coherence in our current scheme. Our experiment provides a set of reservoir-engineering and state-characterization tools to study quantum optics and implement multimode bosonic codes in superconducting circuits.

DOI: [10.1103/PRXQuantum.4.020319](https://doi.org/10.1103/PRXQuantum.4.020319)

I. INTRODUCTION

The use of continuous-variable states of bosonic modes as a platform for quantum information processing, originating in quantum optics [1,2], is rapidly advancing in superconducting circuit quantum electrodynamics (cQED) [3,4]. While many of the exotic states envisioned decades ago remain challenging to implement in the optical domain, they have become practical and valuable resources in the microwave domain due to the ability to engineer a wide range of mode couplings and nonlinearities in Josephson circuits [5]. For example, the Schrödinger cat states [6–8] and the Gottesman-Kitaev-Preskill (GKP) grid states [9] have not only been realized but also actively pursued for encoding logical qubits with error suppression or correction capabilities.

One interesting class of bosonic states yet to be studied experimentally is the pair-coherent state (PCS), an example of a Barut-Girardello generalized coherent state [10]. This state has gained theoretical interest as an example of a highly entangled two-mode state [11,12] and was initially proposed to explain a suppression of amplified spontaneous emission in an atomic system [13]. Analogous to the Glauber coherent state, $|\alpha\rangle = \mathcal{N} \sum_{n=0}^{\infty} \alpha^n / \sqrt{n!} |n\rangle$, a PCS can be written in the Fock-state basis of two harmonic oscillators (a and b) as

$$|\gamma, \delta\rangle = \mathcal{N} \sum_{n=0}^{\infty} \frac{\gamma^{n+\delta/2}}{\sqrt{n!(n+\delta)!}} |n+\delta\rangle_a |n\rangle_b, \quad (1)$$

where δ is an integer describing the photon-number difference (PND) between the two modes, γ is a complex number describing the amplitude and phase of the state, and \mathcal{N} is a normalization factor. This state is both an eigenstate of the pair-photon annihilation operator $\hat{a}\hat{b}$ and the PND operator $\hat{\delta} = \hat{a}^\dagger \hat{a} - \hat{b}^\dagger \hat{b}$:

$$\hat{a}\hat{b} |\gamma, \delta\rangle = \gamma |\gamma, \delta\rangle, \hat{\delta} |\gamma, \delta\rangle = \delta |\gamma, \delta\rangle. \quad (2)$$

A PCS is inseparable and already in the form of a Schmidt decomposition [12]. The $|\gamma, 0\rangle$ state resembles a two-mode squeezed state in terms of photon-number correlation [14]

*wangc@umass.edu

†These authors contributed equally to this work.

Published by the American Physical Society under the terms of the [Creative Commons Attribution 4.0 International](https://creativecommons.org/licenses/by/4.0/) license. Further distribution of this work must maintain attribution to the author(s) and the published article's title, journal citation, and DOI.

but has a Poisson-like photon-number distribution approximately centered around γ .

PCSs form the basis of a recently proposed quantum error-correction (QEC) code called the pair-cat code [15]. This code promises autonomous QEC of all types of first-order physical errors associated with loss and dephasing by encoding a logical qubit in the superposition of PCSs $|\pm\gamma, \delta\rangle$ of two oscillators. The scheme involves stabilizing PND to correct the quantum jumps of photon loss events while simultaneously stabilizing the PCS manifold with a two-mode four-photon dissipation process.

Despite progress in universal control [16–18] and measurement feedback [9, 19–21] in bosonic cavity systems, there is a clear need for new tools for multimode quantum operations. For example, unitary preparation of a PCS using a dispersively coupled ancilla qubit with the current standard technique, numerical optimal control pulses [16], becomes prohibitively difficult for modest photon numbers. On the other hand, reservoir engineering [22] has been of particular interest for its ability to stabilize nonclassical oscillator states in a resource-efficient manner [23]. Moreover, engineered dissipation can provide us with not only encoded qubits with high noise bias [15, 24] but also a set of bias-preserving gates for hardware-efficient quantum computing [25–28]. In cQED, realization of nonlinear dissipation operators have led to stabilization of the cat-state manifolds [29–31] and autonomous QEC of photon losses [32] in a single cavity. However, engineered nonlinear dissipation across two cavity modes remains to be explored.

Similarly, characterization of multimode bosonic states poses substantial challenges beyond their single-mode counterparts. Although multimode Wigner tomography using joint parity or joint photon-number measurements has been previously demonstrated [7, 18, 33, 34], such a process shares similar scalability challenges as in multiqubit state tomography and additionally lacks the convenience to arrange an orthogonal measurement basis for efficient information extraction. In order to explore the space of multimode bosonic QEC codes such as the pair-cat code or the two-mode binomial [35, 36] and GKP codes [37], it is crucial to develop efficient tools to characterize the relevant metrics of the states.

In this work, we present an experimental realization of the PCS and efficient characterization of its coherence. We expand the toolbox of quantum reservoir engineering by realizing an effective dissipation operator that removes photon pairs from two superconducting cavities and stabilizes the complex amplitude of the PCS. This pair-photon dissipation is realized using a pumped superconducting transmon ancilla for nonlinearity and a short-lived oscillator mode as the reservoir. To characterize the two-cavity state, we use three levels of the transmon ancilla to isolate selected subspaces of the large Hilbert space before Ramsey-style tomographic measurements. We use this

subspace-tomography technique to independently measure the quantum coherence between individual pairs of Fock components of the two-cavity state. Our characterization reveals the phase distortion and limited coherence of the stabilized PCS, which we attribute to the spurious cavity-reservoir cross-Kerr interactions. We further demonstrate an effective method of measuring the PND without fine matching of system parameters, which may be used for discrete or continuous tracking of error syndromes in future implementation of the pair-cat code.

This paper is organized as follows. In Sec. II, we discuss a model of the pair-photon driven-dissipation process in our cQED system while introducing our experimental setup. In Sec. III, we present experimental characterization of our PCS stabilization process. This includes measurements of the pair-photon population dynamics, direct PND measurements, a demonstration of manifold stabilization, and joint Wigner tomography. In Sec. IV, we introduce and implement the subspace tomography that leads to quantitative understanding of the nonideality of the stabilized PCS. We conclude in Sec. V with a brief summary and outlook.

II. PCS STABILIZATION SCHEME IN cQED

Our approach to generating and stabilizing a PCS is based on the application of a pair-photon drive counterbalanced by engineered pair-photon dissipation and a cross-Kerr interaction. To understand how the PCS naturally emerges as the steady state under their combined effect, the two-mode system dynamics can be compared or mapped to (1) the textbook example of the stabilized Glauber coherent state of a driven damped oscillator, and (2) previous demonstrations of stabilized single-mode cat-state manifolds [8, 29]. The correspondence of relevant Hamiltonian and dissipator terms are listed in Table I.

While the pair-photon drive $\hat{H}_d = \epsilon_{ab}\hat{a}^\dagger\hat{b}^\dagger + c.c.$, also known as the two-mode squeezing drive [40], has long been a workhorse in quantum optics, stabilization of the PCS requires either a strong (nonunitary) pair-photon loss mechanism or a strong (unitary) cross-Kerr interaction (strong relative to the single-photon decay rates). These two possible strategies are analogous to the stabilized “dissipative cat” [29, 31] and “Kerr cat” [8, 41], respectively, in the single-mode two-photon processes. In fact, the dissipative and unitary effects play the roles of real and imaginary components of the restoring force and are mutually compatible (see Table I). Inspired by both types of cat-state stabilization, our system combines both effects while generalizing this coherent stabilization to the two-mode scenario. The three-dimensional (3D) cQED architecture is ideal for realizing this driven-dissipation process due to the availability of strong coupling between modes, the four-wave-mixing (FWM) capability of the Josephson junction, and the wide range of mode lifetimes achievable in the same system.

TABLE I. A comparison of multiphoton steady states under driven dissipative processes constructed with different operators, $\hat{o} = \hat{a}, \hat{a}^2$ and $\hat{a}\hat{b}$. For each of the three cases, we consider cavity dynamics following the master equation $\dot{\rho} = -\frac{i}{\hbar}[\hat{H}_0 + \hat{H}_d, \rho] + \mathcal{D}(\rho)$ written in the rotating frame of the drives, where \mathcal{D} is the Lindblad superoperator with \hat{o} as its jump operator. In the textbook example of the driven damped quantum oscillator, the mode detuning Δ and single-photon loss κ jointly counter the driving force and determine the complex amplitude of the unique steady state of the system. In two-photon dynamics, the complex amplitude of the steady states is analogously determined by the one-mode or two-mode squeezing drives countered by the corresponding two-photon loss rates and confining Kerr Hamiltonian [38]. Our experiment produces PCSs under both dissipative and cross-Kerr Hamiltonian confinement, with the effective cross-Kerr K_{eff} a few times stronger than the pair dissipation κ_{ab} . Notably, two steady states exist (with even or odd photon-number parity Π) for the case of cat-state stabilization, while there are infinitely many steady states (with different photon-number difference δ) for the case of stabilizing PCSs.

Process category	Drive Hamiltonian \hat{H}_d/\hbar	Dissipator \mathcal{D}	Hamiltonian \hat{H}_0/\hbar	Steady state(s)
Single-photon	$\epsilon^* \hat{a} + \epsilon \hat{a}^\dagger$	$\kappa \mathcal{D}[\hat{a}]$	$\Delta \hat{a}^\dagger \hat{a}$	Coherent state $ \alpha\rangle$, $\alpha = \frac{\epsilon}{i\kappa/2 - \Delta}$
Single-mode two-photon	$\epsilon_2^* \hat{a}^2 + \epsilon_2 \hat{a}^{\dagger 2}$ [39]	$\kappa_2 \mathcal{D}[\hat{a}^2]$ [29]	$K_a \hat{a}^{\dagger 2} \hat{a}^2$ [8]	Cat states $ \alpha, \Pi = \pm 1\rangle$, $\alpha = \sqrt{\frac{\epsilon_2}{i\kappa_2/2 - K_a}}$
Two-mode pair-photon	$\epsilon_{ab}^* \hat{a}\hat{b} + \epsilon_{ab} \hat{a}^\dagger \hat{b}^\dagger$ [40]	$\kappa_{ab} \mathcal{D}[\hat{a}\hat{b}]$	$K_{\text{eff}} \hat{a}^\dagger \hat{a} \hat{b}^\dagger \hat{b}$	PCSs $ \gamma, \delta \in \mathbb{Z}\rangle$, $\gamma = \frac{\epsilon_{ab}}{i\kappa_{ab}/2 - K_{\text{eff}}}$

As shown in Fig. 1(a), our system contains two cylindrical-post cavity modes a and b (with single-photon loss rates $\kappa_a/2\pi = 0.30$ kHz and $\kappa_b/2\pi = 0.74$ kHz), a strip-line resonator r (with decay rate $\kappa_r/2\pi = 0.78$ MHz) used for readout and as a Markovian reservoir, and an ancilla transmon q . The device architecture is similar to that in Ref. [7] except that the two cavity posts share the same elliptical cavity body to allow strong transmon-cavity couplings with a relatively small transmon antenna (see Appendix A). The cavity and resonator modes have annihilation operators \hat{a} , \hat{b} , and \hat{r} . The leading-order terms of the static system Hamiltonian in the rotating frame are

$$\hat{H}_0 = \hat{H}_{\text{disp}} + \hat{H}_{\text{sk}} + \hat{H}_{\text{rk}}, \quad (3)$$

where

$$\hat{H}_{\text{disp}}/\hbar = - \sum_{m=a,b,r} (\chi_m |e\rangle \langle e| + \chi_m^f |f\rangle \langle f|) \hat{m}^\dagger \hat{m} \quad (4)$$

are the dispersive interaction terms between the lowest three transmon levels ($|g\rangle, |e\rangle, |f\rangle$) and the cavity and resonator modes, which we use for characterization of the cavity bosonic states,

$$\hat{H}_{\text{sk}}/\hbar = -K_{aa} \hat{a}^\dagger \hat{a} \hat{b}^\dagger \hat{b} - \frac{K_{aa}}{2} (\hat{a}^\dagger \hat{a})^2 - \frac{K_{bb}}{2} (\hat{b}^\dagger \hat{b})^2 \quad (5)$$

are the cross-Kerr and self-Kerr nonlinearities of the storage cavities, and

$$\hat{H}_{\text{rk}}/\hbar = -(K_{ar} \hat{a}^\dagger \hat{a} + K_{br} \hat{b}^\dagger \hat{b}) \hat{r}^\dagger \hat{r} - \frac{K_{rr}}{2} (\hat{r}^\dagger \hat{r})^2 \quad (6)$$

are the Kerr terms involving the reservoir mode, which are spurious nonlinearities in this experiment. The device is measured in a dilution refrigerator at a nominal base temperature of 20 mK. All device parameters are listed in

Table II (see Appendix A), with the general rates hierarchy of $\chi_m \gg \kappa_r \gg K_{mn} \gg \kappa_{a,b}$ (where $m, n = a, b, r$).

To implement the pair-photon excitation and dissipation, we apply two stabilization drives to our system: a strong off-resonance FWM pump that coherently converts reservoir photons with pairs of photons in a and b and a

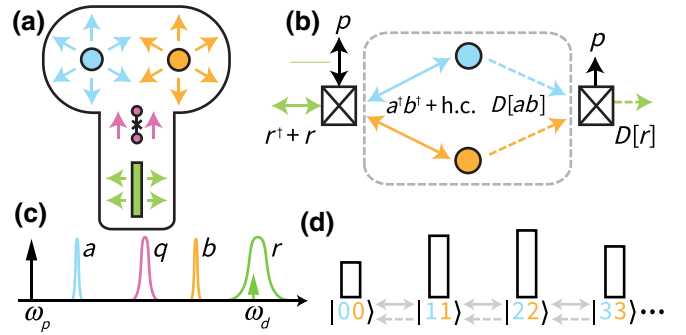


FIG. 1. PCS generation: the system and protocol. (a) Cartoon of the 3D cQED system containing two high- Q cylindrical-post cavities a and b (blue and orange), the transmon ancilla q (magenta), and the strip-line low- Q reservoir r (green). (b) The four-wave mixing pump p , with frequency $\omega_p \approx \omega_a + \omega_b - \omega_r$, coherently converts reservoir excitations with pairs of a and b excitations mediated by the ancilla junction. The ancilla junction also converts the reservoir decay (dotted green arrow) into an effective pair-photon dissipative process (dotted blue and orange arrows). Note that the two drawings of the junction depict what happen with the same junction. After adiabatic elimination of the reservoir, the storage-cavity dynamics are shown in the dotted box. (c) Cartoon of the mode frequencies and line widths (not to scale). The strong off-resonance pump tone p and the weak on-resonance ($\omega_d \approx \omega_r$) reservoir drive d are shown as vertical arrows. (d) A schematic diagram of $\delta = 0$ states under pair-photon drive (double-headed arrow) and pair dissipation (dotted arrow). Fock states are written as $|n_a n_b\rangle$ and the vertical bars represent a PCS distribution.

weaker drive approximately on resonance with the reservoir [Figs. 1(b) and 1(c)]. Under these two drives, the Hamiltonian gains an interaction term under the rotating-wave approximation:

$$\hat{H}_{\text{int}}/\hbar = g_{ab}\hat{a}^\dagger\hat{b}^\dagger\hat{r} + \epsilon_d\hat{r}^\dagger + \text{h.c.}, \quad (7)$$

where ϵ_d is the rate of the reservoir drive and g_{ab} is the four-wave mixing rate activated by the off-resonance pump. If we assume that the transmon remains in the ground state and then adiabatically eliminate the reservoir due to its fast relative dynamics, we obtain a Lindblad master equation for the reduced density matrix ρ of the two storage cavities:

$$\begin{aligned} \frac{\partial \rho}{\partial t} = & -\frac{i}{\hbar}[(\epsilon_{ab}\hat{a}^\dagger\hat{b}^\dagger + K_{\text{eff}}\hat{a}^\dagger\hat{a}\hat{b}^\dagger\hat{b} + \text{h.c.}), \rho] \\ & + \mathcal{D}[\sqrt{\kappa_{ab}}\hat{a}\hat{b} + \zeta_a\hat{a}^\dagger\hat{a} + \zeta_b\hat{b}^\dagger\hat{b}](\rho), \end{aligned} \quad (8)$$

where we combine the storage Kerr terms (\hat{H}_{sk}) as a single K_{eff} term (valid in the limit of $\gamma \gg \delta$). $\mathcal{D}[\hat{o}](\rho)$ is the Lindblad superoperator with a composite jump operator $\hat{o} = \sqrt{\kappa_{ab}}\hat{a}\hat{b} + \zeta_a\hat{a}^\dagger\hat{a} + \zeta_b\hat{b}^\dagger\hat{b}$, where ζ_a and ζ_b are complex coefficients related to \hat{H}_{rk} . In the limit of $g_{ab} \gg K_{ar}, K_{br}$, ζ_a and ζ_b become negligible, this jump operator is reduced to the desirable form of two-photon loss, $\hat{o} \propto \hat{a}\hat{b}$, and the system is stabilized to the PCS manifold as described in Table I.

Unlike previous analyses of two-photon driven dissipation [29,31], we emphasize that Eq. (8) is valid even when the reservoir mode is driven far away from vacuum (i.e., displaced to a large coherent state when $\epsilon_d > \kappa_r$) as long as the adiabatic condition, $\kappa_r \gg g_{ab}, K_{mn}$, is satisfied. The effective pair-photon drive ϵ_{ab} and pair-photon loss rate κ_{ab} both increase with the four-wave mixing rate, $\epsilon_{ab} = -2ig_{ab}\epsilon_d/\kappa_r$, $\kappa_{ab} = 4|g_{ab}|^2/\kappa_r$, while only the pair-photon drive increases with the reservoir drive. Unexpectedly, at least initially, the reservoir nonlinearity, \hat{H}_{rk} , enters as dephasinglike modifications added to the pair-photon loss operator $\sqrt{\kappa_{ab}}\hat{a}\hat{b}$ in Eq. (8), which contributes significantly to the experimental outcome. For the analytical derivation of the system dynamics, see Appendix B.

III. GENERAL CHARACTERIZATION OF PAIR-PHOTON STABILIZATION

A. Pair-photon population dynamics

To characterize the pair-photon-driven dissipative dynamics, we first measure the two-cavity photon-number distributions for any prepared state. To do this, we perform spectroscopy of the ancilla transmon, the frequency of which is shifted by $-\chi_{a,b}$ for every photon in cavity a or b . A frequency-selective rotation of the ancilla at a detuning $\Delta\omega_q = -n_a\chi_a - n_b\chi_b$ maps the probability of

being in Fock state $|n_a n_b\rangle$ to the ancilla excitation, which can then be read out. Here, we write the two-cavity Fock state $|n\rangle_a \otimes |m\rangle_b$ as $|nm\rangle$ in short, a convention that is used for the rest of the paper. To find an optimal condition to create a PCS in the presence of an ac Stark shift, we sweep the frequency of the four-wave mixing pump while measuring probabilities of various $\delta = 0$ photon-number states [Fig. 2(b)]. After 15 μs of pumping with calibrated drive rates of $g_{ab}/2\pi = 60$ kHz and $\epsilon_d/2\pi = 780$ kHz, we observe the full spectroscopy of the ancilla [Fig. 2(c)], which illustrates the Poisson-like distribution of a PCS. We can also track these photon population probabilities over time to understand how the system converges to a quasisteady state with a pair-photon drive and pair-photon dissipation [Fig. 2(d)] or how it decays under the pair-photon dissipation alone [inset of Fig. 2(d)]. The spectroscopy measurements use ensemble-averaged dispersive readout, where the complex transmission coefficient of the readout pulse (at frequency ω_r) is converted to the population of various cavity states through a normalization procedure as described in Appendix A.

Fitting these time-domain data of pair-photon population dynamics to numerical simulations of Eq. (8) (see Appendix C), we extract the pair-photon dissipation rate $\kappa_{ab}/2\pi = 12.5$ kHz (from Fig. 2(d), inset) and subsequently the pair-photon drive rate $\epsilon_{ab}/2\pi = 99$ kHz [from Fig. 2(d)], in good agreement with values expected from adiabatic elimination. Together with the effective cross-Kerr of the system ($K_{\text{eff}}/2\pi = -86$ kHz), these rates are significantly faster than the undesirable single-photon loss rates κ_a and κ_b . Therefore, we experimentally create a quasisteady state resembling a PCS with $|\gamma| = 2.3$ and $\delta = 0$ under these driven-dissipation conditions. Single-photon loss eventually decoheres the state by altering δ over a time scale dictated by the combined cavity lifetimes and average photon numbers (estimated to be about 80 μs here).

We note that different combinations of n_a and n_b can, in principle, result in a similar dispersive shift to the ancilla, causing ambiguity in our measurement of the cavity-photon population. However, for our system with $3\chi_{qa} \approx \chi_{qb}$, this ambiguity arises only when the underlying Fock state $|n_a n_b\rangle$ deviates from its expected δ by at least 4, which is highly unlikely to occur over time scales shorter than the single-photon losses.

A prominent feature of the population dynamics in Fig. 2(d) is oscillations between states, which are then damped to a steady state. The oscillations arise from the underdamped Kerr dynamics of the storage cavities, $\kappa_{ab} < |K_{\text{eff}}|$, and are due to the sudden turn-on of the stabilization drives not allowing the storage cavities to adiabatically evolve in the ground state of the Kerr Hamiltonian as in Ref. [8]. Nevertheless, the pair-photon dissipation plays a crucial role in relaxing the system to the steady state, allowing us to bypass the otherwise slow

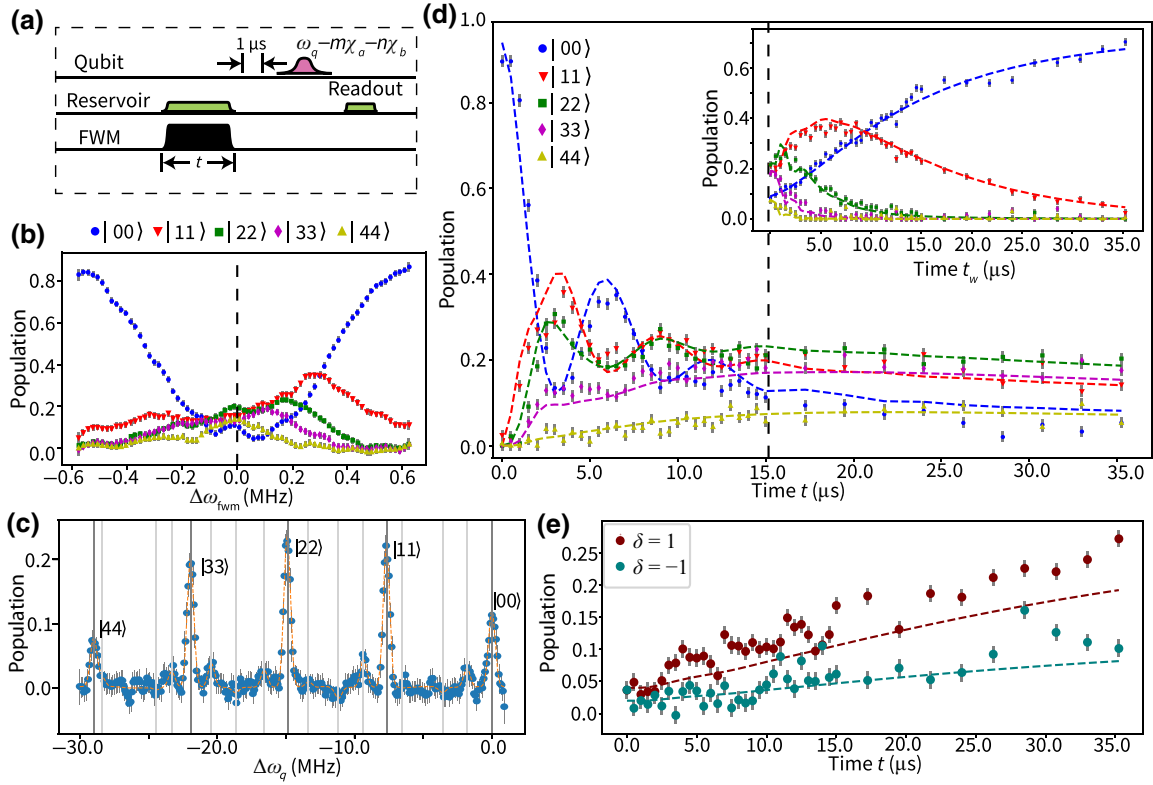


FIG. 2. PCS characterization: the population and time dynamics. (a) A pulse sequence using selective ancilla rotation to analyze the photon population dynamics. We use an ancilla π pulse with a frequency as shown to measure the population of a two-cavity state $|mn\rangle$ after waiting for $1 \mu\text{s}$ for the reservoir to relax. (b) The populations of two-cavity states $|00\rangle$ through $|44\rangle$ after pumping a vacuum state for $t = 15 \mu\text{s}$ at different FWM pump frequencies (while keeping the reservoir drive constant). The remaining experiments are carried out under the condition shown as $\Delta\omega_{\text{fwm}} = 0$ here. (c) Transmon spectroscopy after $15 \mu\text{s}$ of pumping with cw FWM and reservoir tones. The dark vertical lines correspond to $\delta = 0$ states while the light vertical lines correspond to error states caused by single-photon loss. (d) Time-domain photon population measurements with both cw tones applied for a variable time t . The inset shows a time-domain measurement of the pair-photon decay (without pair-photon drives) by keeping only the FWM pump on for a variable amount of time after the two-tone pumping for $t = 15 \mu\text{s}$ (vertical dashed line). The dashed curves are numerical fits to the pair-photon dynamics model [see Eq. (8)] plus single-photon losses, including only two free parameters: $\epsilon_{ab}/2\pi = 99 \text{ kHz}$ and $\kappa_{ab} = (12.7 \mu\text{s})^{-1}$. (e) Measurement of the photon-number difference δ , where the probability of $\delta = \pm 1$ is measured over variable time t to show the effects of single-photon loss from the storage cavities. The nonzero initial populations are due to imperfect cavity reset. The dashed lines are simulation results with the same parameters as in (d). Note that all population values are inferred from a normalized readout procedure (applies to all figures), as discussed in Appendix A.

ramping of the pump tones required for adiabatic state preparation. This hybrid implementation of dissipation and Hamiltonian stabilization is analogous to recent proposals of combining Kerr-cat qubits with engineered dissipation to further improve robustness against unwanted excitations [25,38,42]. The spurious dephasinglike contributions in the jump operator in Eq. (8) also contributes to the convergence to a steady state, which, however, is accompanied with loss of coherence, as is discussed later.

B. Measurement of photon-number difference

Single-photon loss is a fundamental decoherence channel in superconducting cavities that is not stabilized by the pair-photon-driven dissipation. Quantum nondemolition

measurement of PND followed by autonomous or digital feedback is a crucial component of the pair-cat QEC code [15]. An existing proposal for PND measurement requires an exact negative χ -matching condition, $\chi_a = -\chi_b$, which allows direct mapping of the probability of the two-cavity state in a targeted δ onto the ancilla excitations via a simple selective rotation [15]. For a transmon ancilla, this negative χ -matching condition does not occur naturally but can be achieved with additional strong off-resonant pumps [43]. It should be noted that managing multiple strong off-resonant pumps in cQED devices without incurring instabilities remains an active challenge [44].

Here, we demonstrate an alternative method of PND measurement without χ matching. We apply a comb of number-selective π pulses to excite the ancilla at

frequencies corresponding to the dispersive shifts for all cavity states (below a reasonable truncation) with a targeted δ . Subsequent readout of the ancilla informs whether or not the PND of the two-cavity state is equal to δ . For instance, we could superimpose pulses at $\omega_q - n\chi_a - (n+1)\chi_b$, where $0 \leq n \leq 5$, to inquire whether the system is in $\delta = -1$. In Fig. 2(e), we use this measurement to probe the populations in the $\delta = \pm 1$ states, which shows the effect of single-photon loss. While our experimental setup does not have a quantum-limited amplifier to perform the necessary demonstration, this technique of PND measurement is, in principle, quantum nondemolition as long as the phases of the π pulses are tuned to be effectively equal after compensating for any ac Stark shift and Kerr effects. It can then be used to repetitively monitor single-photon loss from a state with known δ so long as $|00\rangle$, $|10\rangle$, and $|01\rangle$ are number resolved and a recovery operation can be applied before the next photon loss occurs. Therefore, it provides a practical avenue for QEC of single-photon loss in the pair-cat code, hence relaxing one of its demanding requirements for implementation. The comb-based PND measurement may also be converted to an autonomous QEC protocol to correct photon-loss errors [32]. However, without the negative χ -matching condition, this simple and effective method of PND mapping is not fault tolerant with respect to ancilla T_1 error, which may require other means of protection.

C. Manifold stabilization

An important property of the pair-photon driven-dissipation process is conservation of the photon-number difference δ : it stabilizes γ while allowing δ to be the one and only degree of freedom inherited from arbitrary initial values and it may allow quantum operations in the presence of stabilizing pumps. For example, the photon-number distribution in Fig. 2 corresponds to the unique steady state of the two-cavity system within the $\delta = 0$ subspace and its δ is inherited from the initial vacuum state before the pair-photon pumping is applied. To create a PCS with $\delta = 1$ or -1 , we can use a selective number-dependent arbitrary-phase (SNAP) gate [45] to prepare a $|10\rangle$ or $|01\rangle$ initial state before applying the same pumping conditions. The resultant photon-number distributions are shown in Fig. 3, corresponding to PCSs of $|\delta = 1, |\gamma| \approx 2.4\rangle$ and $|\delta = -1, |\gamma| \approx 2.2\rangle$, respectively. More generally, the pair-photon dynamics of Eq. (8), in the ideal limit of $\zeta_a, \zeta_b = 0$, confine the two-cavity state to a quantum manifold (Hilbert subspace) spanned by a series of PCSs with a fixed γ and an arbitrary integer δ . Any coherent superpositions of these PCSs are steady states allowed by the driven dissipation, although the coherence is not protected against single-photon loss, which shifts the value of δ between neighboring integers.

D. Joint Wigner measurements

To demonstrate the nonclassicality and coherence of these stabilized states, we measure the joint Wigner function of the two-cavity state ρ [46]:

$$W(\alpha, \beta) = \frac{4}{\pi^2} \text{Tr}[\rho \hat{D}_a(\alpha) \hat{D}_b(\beta) \hat{P}_J \hat{D}_b^\dagger(\beta) \hat{D}_a^\dagger(\alpha)], \quad (9)$$

where $\hat{P}_J = e^{\pi i(\hat{a}^\dagger \hat{a} + \hat{b}^\dagger \hat{b})}$ is the joint photon-number parity operator and $\hat{D}_a(\alpha)$ and $\hat{D}_b(\beta)$ are the phase-space displacement operators of the two cavities, respectively. We take advantage of our approximately matched dispersive shift of the $|e\rangle$ - $|f\rangle$ transmon transition, $\chi_a^f - \chi_a = \chi_b^f - \chi_b$, to measure the joint photon-number parity, the expectation value of which following cavity displacements in the four-dimensional (4D) phase space (α, β) can be directly scaled to the joint Wigner function [7,47].

In Fig. 4(b), with a two-dimensional (2D) angular cut of the joint Wigner function at fixed displacement amplitudes, we first demonstrate an interesting property of PCSs (or any eigenstates of $\hat{\delta}$ in general): invariance with respect to the differential cavity phase $W(\alpha, \beta) = W(\alpha e^{i\phi}, \beta e^{-i\phi})$. This is because the product of the cavity rotation operators $\hat{R}_a(\phi) \hat{R}_b(-\phi) = e^{i\phi \hat{a}^\dagger \hat{a}} e^{-i\phi \hat{b}^\dagger \hat{b}} = e^{i\phi \hat{\delta}} \equiv \mathbb{I}$ for a PCS up to a global phase. On the other hand, oscillation with respect to the total phase is a signature of phase coherence of the two-cavity state. Choosing the common phase

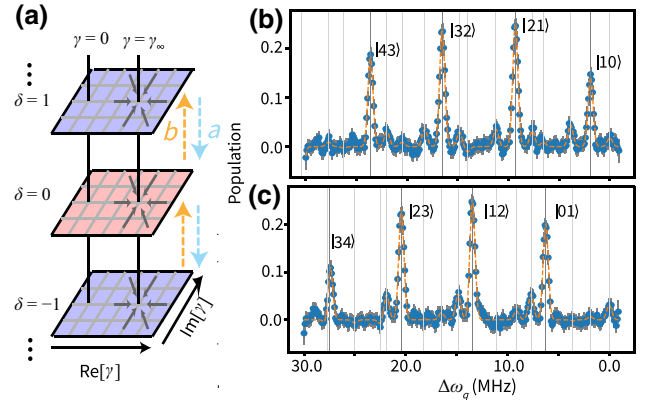


FIG. 3. The manifold of stabilized PCSs. (a) A conceptual representation of the different δ subspaces of the two-cavity system under pair-photon-driven dissipation. Each subspace has a unique steady state $|\gamma_\infty, \delta\rangle$, which functions as an attractor in a generalized phase plane. In general, the system is stabilized to the manifold of states represented by the vertical string $\gamma = \gamma_\infty$. (b),(c) Ancilla spectroscopy that demonstrates the photon-number distribution of the stabilized (b) $\delta = 1$ and (c) $\delta = -1$ PCSs. These measurements are performed by preparing initial states of $|10\rangle$ and $|01\rangle$, respectively, and then applying the exact same stabilization drives as used in Fig. 2(c) for $t = 15 \mu\text{s}$. For each plot, the dark vertical lines indicate the desired states while the light vertical lines mark error states due to single-photon loss or imperfect initial-state preparation.

$1/2(\arg[\alpha] + \arg[\beta])$ where the Wigner function takes the maximum value, we show measured 2D phase-space cuts of the joint Wigner function of the experimental $\delta = 0, +1$, and -1 PCSs to be compared to the closest-matched ideal PCS [Figs. 4(d)–4(i)]. These Wigner data are acquired after $t = 15 \mu\text{s}$ of stabilizing drives and an additional $t_w = 4.5 \mu\text{s}$ of wait time. We note that $t_w \gtrsim 5/\kappa_r = 1 \mu\text{s}$

is necessary to allow the reservoir photons to fully decay and the wait time here is chosen to reach the first phase revival of an approximate PCS after cavity Kerr dynamics [48]. The characteristic interference fringes of the PCS are clearly visible, indicating appreciable coherence and consistent multiphoton phases. The even-parity ($\delta = 0$) and odd-parity ($\delta = \pm 1$) states show opposite Wigner contrasts

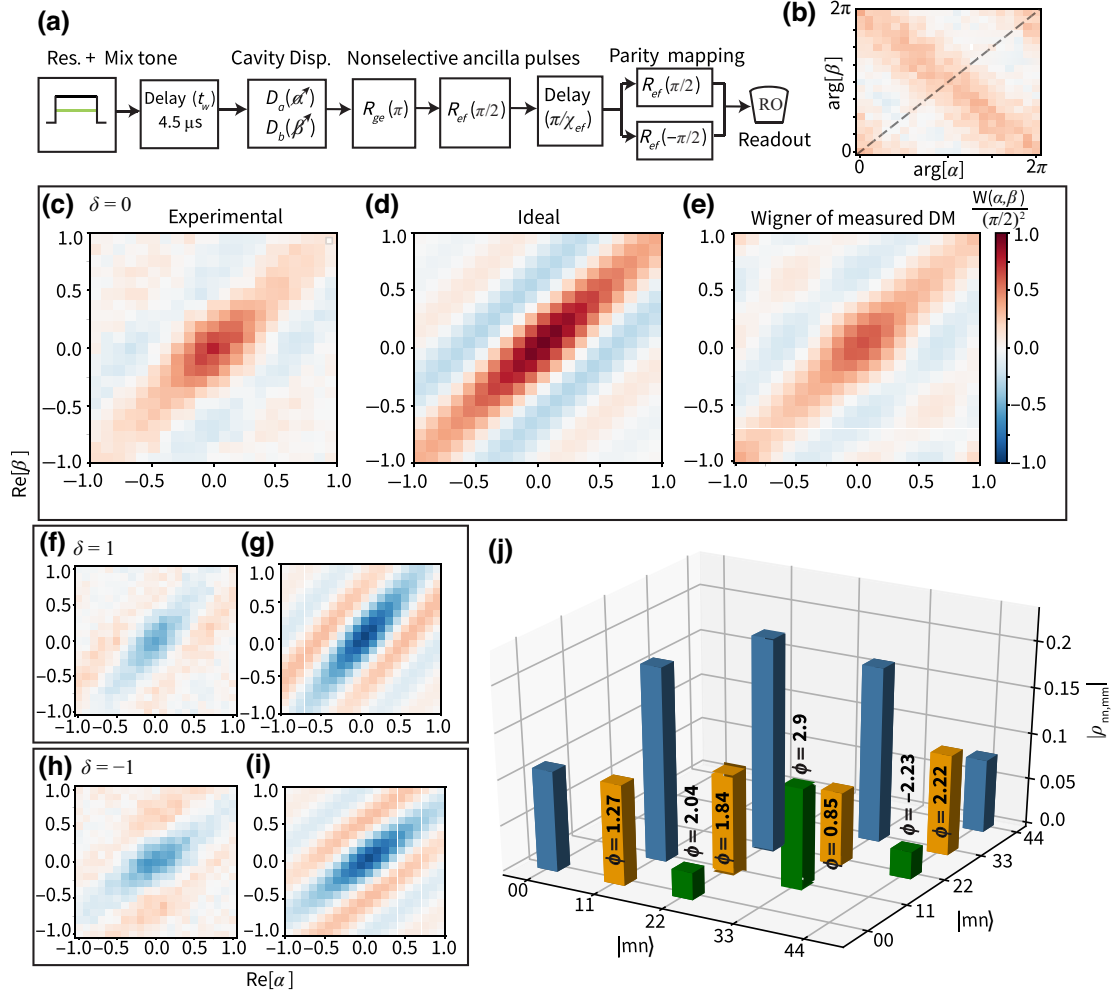


FIG. 4. The joint Wigner tomography of PCSs. (a) The pulse sequence for Wigner-function measurements. The two cw tones are applied for $t = 15 \mu\text{s}$ to prepare and stabilize a state that is then evolved under no pump tones for $t_w = 4.5 \mu\text{s}$ to reach the first phase revival of an approximate PCS under cavity Kerr dynamics (and for the reservoir to relax to vacuum). The joint parity mapping uses a Ramsey sequence with an evolution time of π/χ_{ef} , where $\chi_{ef} \approx \chi_a^f - \chi_a \approx \chi_b^f - \chi_b$. (b) The Wigner function, $\frac{\pi^2}{4} W(\alpha, \beta)$, of the stabilized $\delta = 0$ state with constant displacement amplitudes $|\alpha| = |\beta| = 0.3$ and sweeping over the angle of both displacements. (c) The measured $\text{Re}[\alpha]$ - $\text{Re}[\beta]$ cut of the joint Wigner function for the approximate $|\gamma = 2.3, \delta = 0\rangle$ PCS (with the real axes redefined such that $\arg[\gamma] = 0$). This can be compared to the same Wigner-function cuts of (d) the ideal PCS $|2.3, 0\rangle$ and (e) the experimentally measured density-matrix block [as shown in (j)] of this stabilized state. (f),(h) The measured $\text{Re}[\alpha]$ - $\text{Re}[\beta]$ cut of the joint Wigner function for the approximate $|\gamma = 2.4, \delta = 1\rangle$ and $|\gamma = 2.2, \delta = -1\rangle$ PCSs stabilized under the same condition, to be compared to (g),(i) the corresponding ideal PCSs, respectively. (j) The $\delta = 0$ block of the density matrix of the stabilized $\delta = 0$ state at the same effective free-evolution time, measured with quantum subspace tomography (note that this is independent from the Wigner measurements) as discussed in Sec. IV. The blue bars are the diagonal elements indicating the population distribution, whereas the off-diagonal coherence elements are shown by orange (green) for nearest (next-nearest) neighboring Fock-state pairs. Other coherence elements are small and hence are not measured in the experiment. The phases of the coherence elements are shown numerically over the bars.

as expected, and the differences in the slope of the fringes are striking features indicating the different PNDs of the states.

The technique of direct joint Wigner tomography in principle allows full reconstruction of the two-cavity density matrix but faces a multitude of practical challenges. First, tomographic reconstruction requires a very large amount of data. Even if we impose a low cutoff of four photons per cavity, the tomography still requires accurate measurements at a minimum of 625 (typically many more) different phase-space sampling points. Second, the joint parity measurement contains some photon-number-dependent systematic errors caused by the storage-readout cross-Kerr, the sixth-order dispersive shift of the transmon, and nonperfect χ matching for joint parity extraction. Last but not least, even with sufficient brute force, it is challenging to prevent small stochastic and systematic errors from propagating badly in the matrix pseudoinversion problem of reconstruction due to the presence of singularities. In our experiment, primarily to limit spurious readout signals due to a large K_{br} , we limit our cavity displacements to $|\alpha|, |\beta| < 1$ in Wigner-function measurements as in Fig. 4, which contains nearly all the salient features of the PCS. However, a full Wigner reconstruction would require cumulative measurements of highly diluted features over a much larger extent of the 4D phase space.

IV. QUANTUM SUBSPACE TOMOGRAPHY

Quantitative insight into our experimental two-cavity state is enabled by a new characterization tool focusing on specific subspaces of interest. The goal is to completely characterize the projected density matrix $\rho_{SS} = \hat{P}\rho\hat{P}$, with projection operator \hat{P} for subspace S of the system. For d -dimensional subspace S , we only need to perform d^2 measurements for subspace tomography. Using a three-level ancilla, one can effectively isolate S from the rest of the Hilbert space using the $|g\rangle$ - $|e\rangle$ transition of the ancilla, and using the $|e\rangle$ - $|f\rangle$ transition to perform tomography. A general protocol for this method is discussed in Appendix D.

A. Implementation of 2D subspace tomography

We demonstrate this subspace-tomography technique with a direct and self-calibrated measurement of the pairwise coherence between the constituent states of the stabilized $\delta = 0$ state. This approximate PCS state obtained in the experiment [the Wigner-function cut of which is shown in Fig. 4(c)] and its density matrix to be determined are both referred to as ρ_M . In this tomographic protocol, we entangle only two Fock components, e.g., $|11\rangle$ and $|22\rangle$, with $|e\rangle$ of the transmon using number-selective π pulses. Within this 2D subspace, since the diagonal elements of the density matrix, which we denote as ρ_{11} and ρ_{22} , are measured via transmon spectroscopy (Fig. 2), the

complex-valued off-diagonal element $\rho_{11,22}$ is the only unknown. We then displace both cavities $\hat{D}_a(|\alpha|e^{i\phi})\hat{D}_b(|\beta|e^{i\phi})$ with fixed amplitudes (typically $|\alpha|$ and $|\beta| < 0.5$) and vary the common phase ϕ , which redistributes the photon populations in the $|e\rangle$ manifold and shows constructive or destructive interference in each Fock component depending on $\rho_{11,22}$ and ϕ [Fig. 5(b)]. Using number-selective $|e\rangle$ - $|f\rangle$ rotation of the transmon, we can measure the population of any individual target state after displacement, such as $|11e\rangle$, which oscillates as a function of ϕ . Alternatively, we can also measure the oscillation in other observables, such as the joint parity [Fig. 5(c)]. The amplitude and phase of such oscillations can be directly converted to $\rho_{11,22}$ following a comparison with easily calculable properties of the state $D(\alpha, \beta)(\sqrt{\rho_{11}}|11\rangle + \sqrt{\rho_{22}}|22\rangle)$. Repeating the same procedure for different pairs of states, we obtain the $\delta = 0$ block of ρ_M by direct measurement of its individual off-diagonal elements as shown in Fig. 4(j). In practice, we run numerical calculations to find the optimal $|\alpha|$, $|\beta|$, and measurement observable for each pair of states, to maximize the visibility of the oscillations.

Experimental implementation of the subspace-tomography technique requires careful tracking of rotating frames and phase accumulation of different branches of states. To ensure self-consistent phase measurements, we work in the two-cavity rotating frame set by two cw stabilization drives (the drive frame) and require the four frequencies of the tomographic pulses to precisely sum up to 0 (Fig. 10). Since the pulse frequencies for selective transmon rotations have no freedom for adjustment, we apply our fast cavity displacement drives at deliberately detuned frequencies in order to exactly compensate for the irregular detunings of all other tones due to various Stark shifts and higher-order nonlinearity of the system (Appendix E). This strategy allows us to measure the phases of off-diagonal density-matrix elements that are unambiguously defined relative to the two stabilization drives. As shown in Fig. 6(a), following $t = 15\ \mu\text{s}$ pumping, our measured phases of $\rho_{00,11}$, $\rho_{11,22}$, $\rho_{22,33}$, and $\rho_{33,44}$ all evolve over the wait time t_w as expected from the frequencies of the corresponding transitions in the drive frame. Note that their frequencies differ due to the Kerr Hamiltonian of the storage cavities [see Eq. (5)]. Figure 6(b) further shows that the measured phases are constant over extended pumping times t .

A key advantage of this $d = 2$ subspace-tomography technique is that it maps individual density-matrix elements of interest to individual experimental signatures in an intuitive manner, making the experimental uncertainties of the tomographic measurements highly transparent. For example, from the sinusoidal fits in Fig. 5(c), we can unambiguously report the uncertainty of the amplitude (3%) and phase (0.05 radian) for $\rho_{11,22}$, which would be extremely challenging to obtain in traditional tomographic

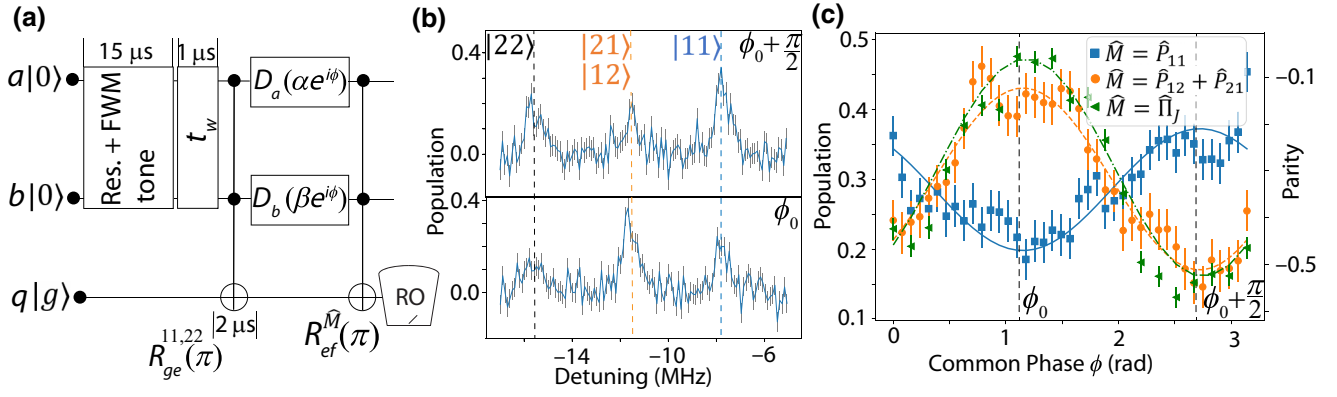


FIG. 5. The subspace-tomography protocol. (a) An example schematic for tomography in subspace $S = \text{span}\{|11\rangle, |22\rangle\}$. Photon-number-selective transmon π pulses (2- μs -long Gaussian) are applied to isolate the two Fock components in the $|e\rangle$ manifold. Cavity displacement pulses are then applied to induce interference, followed by mapping an observable \hat{M} (e.g., the joint parity) to $|f\rangle$. (b) Spectroscopy of the $|e\rangle$ - $|f\rangle$ transition of the transmon after the cavity displacements $\hat{D}_a(|\alpha|e^{i\phi})$ and $\hat{D}_b(|\beta|e^{i\phi})$ in (a) with two different displacement phases $\phi = \phi_0$ and $\phi_0 + \pi/2$, where ϕ_0 is chosen to minimize the $\hat{M} = \hat{P}_{11}$ measurement; thus $\phi_0 + \pi/2$ will maximize it. The difference in photon-number distribution in the two cases demonstrates the presence of interference. The $|21\rangle$ and $|12\rangle$ peaks overlap to appear as a single peak due to the approximately matched dispersive shift of the $|e\rangle$ - $|f\rangle$ transmon transition. Note that the y axis represents the relative fraction of population within the subspace S . (c) The population of $|11\rangle$ (blue), the sum of the populations of $|21\rangle$ and $|12\rangle$ (orange), and the photon-number parity of the displaced state in the $|e\rangle$ manifold (green), all being examples of a general measurement operator \hat{M} , measured as a function of the common displacement phase ϕ . All fit curves correspond to the scaled coherence element $\rho_{11,22}/\sqrt{\rho_{11}\rho_{22}} = 0.63e^{0.84i}$.

reconstruction. Furthermore, it is relatively straightforward to extend our scheme to $d > 2$ by applying more than two selective ancilla π pulses in isolating the subspace, although extra care must be taken in accounting for phase accumulations if the selective pulses are not exactly equally spaced in frequency.

Using the 2D subspace-tomography technique, we can in principle measure the entire density matrix ρ_M element by element. However, since ρ_M is sparse, in practice it is neither efficient nor interesting to measure the vast number of small off-diagonal elements. Since our system dynamics cannot generate superpositions between states of different PNDs, we can write ρ_M in block-diagonal form,

$$\rho_M = \begin{bmatrix} \ddots & & & & \\ & \rho_{[-1]} & & & \\ & & \rho_{[0]} & & \\ & & & \rho_{[1]} & \\ & & & & \ddots \end{bmatrix}, \quad (10)$$

where $\rho_{[\delta]}$ is the projection of ρ onto the subspace with a definite PND of δ . After measuring the population elements and the most prominent coherence elements, we can construct all matrix blocks $\rho_{[\delta]}$ by simply setting unmeasured elements to 0 [Fig. 8(a)] and treat potential deviations from 0 as uncertainties bound by physicality constraints (e.g., off-diagonal elements cannot exceed the geometric mean of corresponding diagonal elements).

Since the state predominantly resides in the $\delta = 0$ subspace described by the extensively measured $\rho_{[0]}$ block [Fig. 4(j)], this treatment is sufficient for extracting various global metrics of the quantum state to a good approximation, such as the fidelity and entanglement measures to be discussed in Sec. IV B.

B. Understanding deviations from an ideal PCS

With the capability of direct pairwise coherence measurements, we can track the amplitude and phase of selected coherence elements in the two-cavity state as a function of the stabilization pumping time t . We find that the cavities indeed converge to a quasisteady state (except for the slow process of single-photon loss) with persistent coherence [Fig. 6(c)]. However, the magnitude of the steady-state coherence is far lower than the ideal values $|\rho_{nn,mm}| = \sqrt{\rho_{nn}\rho_{mm}}$. Moreover, the stabilized cavity phases, which we can extrapolate backward in time from data such as Fig. 6(a), also differ considerably from the ideal PCS, which should have equal superposition phases between neighboring Fock components, i.e., $\arg[\rho_{nn,(n+1)(n+1)}] = \arg[\gamma]$. Due to the Kerr evolution of the storage cavities during idle time ($K_{\text{eff}} = -86$ kHz), we expect a stabilized PCS to collapse and revive every 5.8 μs [48], making $t_w = 5.8$ μs the first optimal timing to observe the PCS in Wigner measurements. However, the measured pairwise phases of the stabilized state suggests that the two-cavity state most resembles a PCS at $t_w \approx 4.5$ μs , which has been confirmed by the joint Wigner

measurements. This skewness in phases and loss of coherence is caused by the relatively large cross-Kerr term of the reservoir mode, $K_{br}/2\pi = 58$ kHz, which is comparable to the competing mixing drive rate $g_{ab}/2\pi = 60$ kHz (while $K_{ar}/2\pi = 7$ kHz is much smaller).

Remarkably, this spurious effect from the reservoir cross-Kerr can be captured well by the simple reduced model of the pair-photon dynamics [see Eq. (8)], which features a composite jump operator $\hat{o} = \sqrt{\kappa_{ab}}\hat{a}\hat{b} + \zeta_a\hat{a}^\dagger\hat{a} + \zeta_b\hat{b}^\dagger\hat{b}$. Through adiabatic elimination of the r mode (Appendix B), we find $\zeta_b = \sqrt{4K_{br}^2 r_0^2 / \kappa_r}$ (and similarly for ζ_a), where r_0 is the complex displacement amplitude of the r mode during the stabilization process. This coefficient is identical to that of photon-shot-noise dephasing of qubits [49], with K_{br} taking the place of the qubit-cavity dispersive shift. Indeed, if the mixing drive is turned off (hence $\kappa_{ab} = 0$), any initial storage-cavity state ρ should be dephased by the fluctuating photon numbers in a driven r mode, which can be described by the usual dephasing jump operators $\hat{a}^\dagger\hat{a}$ and $\hat{b}^\dagger\hat{b}$. In our experiment, $|r_0| = 1.8$, which gives rise to a dephasing rate $|\zeta_b|^2/2 \approx 2\pi \cdot 28$ kHz, while the effect of ζ_a is much less significant. Intuitively, the finite steady-state coherence of the system in Fig. 6 can be understood from the competition between the PCS stabilization mechanism and the spurious dephasing effects.

It is important to note that the pair-photon dissipation and the two dephasinglike terms constitute a single jump operator \hat{o} , not separate ones. This is because the three events are all directly originating from the same

stochastic event of reservoir photon loss. As a result, the relative phases between the terms in \hat{o} play a crucial role in skewing the stabilized state from the ideal PCS, including a larger state size, a broader distribution of photon numbers, and the varying phases between neighboring Fock components. A numerical simulation of Eq. (8) using this composite jump operator reproduces the prominent coherence elements of the pumped two-cavity state, which is in good agreement with the experimental data in Fig. 6, with no free parameters except for a two-cavity global frame rotation of 1.5 rad (which can be attributed to the difference in cable electrical length between the stabilization drive lines and the cavity displacement lines together with a small additional cavity rotation during the reservoir ring-down before the tomography).

For the experimental state ρ_M , we find that its fidelity against the closest ideal $\delta = 0$ PCS $|\psi_0\rangle$ is $\mathcal{F} = \langle\psi_0|\rho_M|\psi_0\rangle = \langle\psi_0|\rho_{[0]}|\psi_0\rangle = 41.5 \pm 1.3\%$. The uncertainty of \mathcal{F} represents one standard error of the mean, which can be directly calculated by combining uncorrelated measurement uncertainties of individual density-matrix elements in $\rho_{[0]}$. Tomographic measurements (or the lack thereof) outside the $\rho_{[0]}$ block do not contribute to \mathcal{F} because the target state $|\psi_0\rangle$ contains no probabilities outside the $\delta = 0$ subspace. Since ρ_M retains about 82% population in $\rho_{[0]}$ (with the rest leaked primarily to $\rho_{[+1]}$ and $\rho_{[-1]}$ due to a single-photon loss) and shows about 50% relative coherence on average between elements in the $\rho_{[0]}$ block (due to the cross-Kerr dephasing previously mentioned), the measured state fidelity is fully explained by these two dominant error channels at play. While this

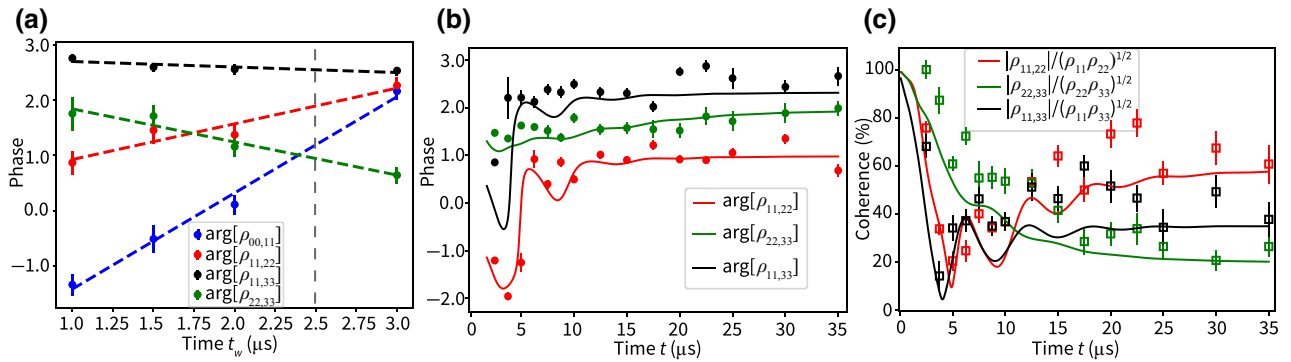


FIG. 6. The evolution of the pair-photon phases and coherence informed by subspace tomography. (a) Phases of selected off-diagonal elements of the two-cavity state ρ_M , measured with the $d = 2$ subspace tomography, as a function of the wait time t_w after state preparation with the stabilizing drives for $t = 15 \mu\text{s}$. The phase evolution agrees with the cavity Kerr terms \hat{H}_{sk} and the cavity detuning in the drive frame. The dashed lines are linear fits, which allow us to interpolate or extrapolate the phases of these states to different t_w . The vertical dashed line corresponds to the time at which the density-matrix block is plotted in Fig. 4(j). In order to compare with Wigner data in Fig. 4, note that the effective free-evolution time of the two-cavity state here is $t_w + 2 \mu\text{s}$, accounting for the duration of the selective transmon $|g\rangle\text{--}|e\rangle$ pulses in the subspace-tomography protocol [Fig. 5(a)]. (b),(c) The (b) phases and (c) relative coherence of selected off-diagonal density-matrix elements of the two-cavity state for different stabilization pumping times t , measured with subspace tomography after $t_w = 1 \mu\text{s}$. The solid lines show parameter-free numerical-simulation results of the storage pair-photon dynamics according to Eq. (8), which does not contain the reservoir mode and captures all prominent features of the data. The two-photon dissipation and drive rates used in the simulation are obtained from the fits in Fig. 2(d).

fidelity indicates a significant need for improvement, we note that our experiment spans a large Hilbert space (i.e., 25 dimensions, assuming a photon-number cutoff of 4 in each cavity) in the context of an initial demonstration of dissipative stabilization of multiphoton entanglement. By comparison, the first studies of dissipatively stabilized entanglement in qubits have reported Bell-state fidelity in the range of 60–70% for a Hilbert space dimension of 4 [50–52].

To quantify entanglement in this nonideal quantum state, we compute the logarithmic negativity, which gives an upper bound on the distillable entanglement. It is defined as $E_N(\rho) = \log_2 \|\rho^{T_a}\|_1$, where T_a is the partial transpose with respect to cavity a and $\|\cdot\|_1$ is the trace norm. If we neglect any coherence within the $\rho_{[\pm 1]}$ blocks of ρ_M for simplicity (i.e., not allowing their off-diagonal elements to vary from 0), we obtain $E_N = 1.05 \pm 0.06$. The likely presence of stabilized coherence within the slightly populated $\rho_{[\pm 1]}$ blocks is found to produce a positive but rather small additional contribution to E_N (up to 0.02 under physicality constraints). Therefore, the measured E_N for our experimental PCS is much smaller than that of an ideal PCS of similar size ($E_N \approx 2.4$) but is already comparable or greater than an ideal Bell pair ($E_N = 1$) despite its very limited coherence.

To improve the quality of the stabilized PCS, it is necessary to suppress the spurious dephasing terms in the composite jump operator \hat{o} . Ideally, this can be accomplished by engineering a Josephson circuit without the reservoir cross-Kerr, analogous to the asymmetrically threaded superconducting quantum interference device (SQUID) circuit for dissipative cat-state stabilization [31]. In our current transmon-based device, this may be accomplished by either an extra Kerr-cancellation pump tone [53] or by detuning the two stabilization drives a few (reservoir) line widths away to reduce photon-number fluctuations in the r mode. The former also suppresses $|K_{\text{eff}}|$ and hence boosts the state size and the dissipative nature of the stabilization scheme. The latter suppresses κ_{ab} and moves our PCS stabilization deeper into the regime relying on Hamiltonian confinement. Given the full understanding of the pair-photon dynamics at the conclusion of this experiment, we believe that both strategies can yield improved fidelity for the stabilized PCS in our device, although new forms of nonlinear ancillas are needed to realize spurious-free pair-photon processes at faster rates.

V. SUMMARY AND OUTLOOK

There is a growing history of cQED experiments inspired by the field of quantum optics. The convenience of microwave systems and the powerful nonlinearity of superconducting circuitry has paved new ways toward the study of exotic bosonic states that may be otherwise prohibitively challenging to implement. Owing to the identical

nature of bosons, bosonic quantum states offer the opportunity of hardware-efficient dissipation engineering schemes but also pose unique challenges requiring new characterization techniques. Both aspects are reflected in our experiments. Unlike earlier demonstrations of two-mode non-Gaussian states such as the entangled cat state [7] or the N00N state [33], the PCS should contain more than one e-bit (EPR pair) of entanglement. It would be interesting to further develop efficient tools to calibrate and distill the entanglement in such states.

The pair-cat code, a recent addition to the zoo of bosonic QEC codes, offers the tantalizing prospect to correct both photon loss and dephasing errors (to the first order) autonomously and fault tolerantly [15]. Our experimental realization of the PCS, demonstration of the first cross-cavity dissipator, and introduction of a convenient (although not fault-tolerant) PND measurement are all valuable steps toward a pair-cat code. However, fully implementing and utilizing the advantages of the pair-cat code will require schemes to suppress forward propagation of ancilla errors and upgrading the pair-photon dissipation to a four-photon cross-cavity dissipator, which involves a leap in experimental complexity.

As a first attempt toward a two-mode bosonic code, our work suggests several challenges moving from one mode to two. Unlike the concatenation of a smaller multiqubit QEC code to a larger one, two-mode bosonic code states generally cannot be created from concatenating single-cavity bosonic qubits using cavity-cavity logic gates. The generation of two-mode states in cQED requires specific cross-cavity nonlinear interactions, which is implemented in our work with a relatively simple hardware setup but not without spurious effects and difficult parameter trade-offs. Future experiments will have to tailor the cross-cavity nonlinear interactions, likely using Josephson circuits with a strong third-order nonlinearity [54], while suppressing unwanted fourth-order terms. In addition, since two-mode states reside in a much larger Hilbert space, their implementation requires both effective confinement to preferred subspaces and efficient methods to diagnose imperfections. With regard to the latter, our work demonstrates a valuable tool in subspace tomography, which provides a general framework for future experiments to isolate key components of a high-dimensional quantum state for characterization.

ACKNOWLEDGMENTS

We thank Michel Devoret, Ioannis Tsioutsios, Akshay Koottandavida, and Yu-Xin Wang for helpful discussions. We thank Juliang Li and Xiaowei Deng for experimental assistance. The device fabrication was supported by the facilities at the UMass Conte Cleanroom and at Amherst

College. This research was supported by the U.S. Department of Energy (Grant No. DE-SC0021099). The fabrication and initial characterization of the device were supported by the Air Force Office of Scientific Research (AFOSR) (Grant No. FA9550-18-1-0092). L.J. would like to acknowledge support from the Army Research Office (ARO) (Grant No. W911NF-18-1-0212), from the AFOSR Multidisciplinary Research Program of the University Research Initiative (MURI) (Grant No. FA9550-19-1-0399), and from the Packard Foundation (2020-71479).

APPENDIX A: EXPERIMENTAL SETUP AND METHODS

1. Device architecture and transmon fabrication

The system consists of two post cavities dispersively coupled to a fixed-frequency transmon ancilla, which is then dispersively coupled to a strip-line $\lambda/2$ resonator that is used for readout and as reservoir in the experiment. The posts are made using high-quality aluminum inside a cavity, as shown in Fig. 7(b). The cavity has a tunnel opening on one of the sides, which is where the sapphire chip containing the qubit and resonator is held with a chip clamp. This high-quality superconducting cavity is made with 5N (99.999%) purity aluminum and it shields the qubit from magnetic field lines that can degrade the coherence. The ancilla qubit and the cavity modes each have their own drive ports. The readout signal is collected from another port that is coupled strongly with the strip-line resonator. The coupling strengths between all the modes and the coherence numbers for the modes are listed in Table II. The setup with the cavities and chip is initially simulated in the electromagnetic solver software ANSYS HFSS to design the frequencies of the modes and interactions between them that are needed for the experiment.

The simulated chip design is fabricated in a cleanroom facility for nanofabrication using the standard procedure. We use a 30-keV JEOL JSM-7001F SEM to perform electron-beam lithography to define the transmon and the strip-line resonator in one step. The aluminum thin film is evaporated on the sapphire chip using Plassys MEB550S. The transmon has a single Al-AlO_x-Al Josephson junction produced by the Dolan-bridge method, where the aluminum is deposited at two different angles while allowing some time in between for it to oxidize.

2. Measurement setup

The measurement setup is designed to generate microwave signals that drive all the four modes in the system and to receive signals from the readout port that are digitized to read the qubit state. We use the basic microwave engineering technique of mixing signals from the signal generator and the arbitrary waveform generator (AWG), using an in-phase and quadrature (IQ) mixer to

modulate the sidebands. The filtered rf output from each mixer then goes into the fridge to the input ports, as shown in Fig. 7(a). The signal collected from the readout port goes to a three-port mixer for demodulation and then to a digitizer. In addition to drives for the modes of the system, the setup also produces a continuous four-wave mixing tone and a reservoir tone that satisfy the frequency-matching condition as discussed in the main text to create a PCS. Inside the fridge, all the input signals are attenuated by 20 dBm at the 4 K plate, 10 dBm at the Still plate, and 30 dBm at the mixing chamber (MXC) and then go through the eccosorb filters (made in house) along with a low pass filter as the last level of filtering before going into the input ports.

We want to study the coherence of the prepared entangled state in the storage cavities by probing them to measure 2D slices of joint Wigner functions as shown in Figs. 4(b)–4(d). The use of different generators to pump and probe the cavities would cause the phase of the state in the storage cavities to not be locked to the cavity displacement drives used to measure the Wigner functions, thus

TABLE II. The measured system parameters.

	Symbol	Value
Transmon frequency	$\omega_q/2\pi$	5378 MHz
Transmon anharmonicity	$\alpha_q/2\pi$	204 MHz
Transmon T_1	T_{1q}	40 μ s
Transmon T_2^* Ramsey	T_{2q}^*	18 μ s
Transmon T_2 echo	T_{2q}	60 μ s
Transmon $ e\rangle_q$ population		2% (3.5% [†])
Reservoir frequency	$\omega_r/2\pi$	7409 MHz
Reservoir-transmon coupling	$\chi_r/2\pi$	3.09 MHz
Reservoir anharmonicity	$K_{rr}/2\pi$	12 kHz
Reservoir decay rate	$\kappa/2\pi$	0.78 MHz
Cavity a frequency	$\omega_a/2\pi$	4072 MHz
Cavity a -transmon $ g\rangle$ - $ e\rangle$ shift	$\chi_a/2\pi$	1.89 MHz
Cavity a -transmon $ g\rangle$ - $ f\rangle$ shift	$\chi_a^f/2\pi$	5.81 MHz
Cavity a anharmonicity	$K_{aa}/2\pi$	8 kHz*
Cavity a T_1	T_{1a}	530 μ s
Cavity a T_2	T_{2a}	400 μ s
Cavity a $ 1\rangle_a$ population		$\sim 2\%$
Cavity b frequency	$\omega_b/2\pi$	6094 MHz
Cavity b -transmon $ g\rangle$ - $ e\rangle$ shift	$\chi_b/2\pi$	6.26 MHz
Cavity b -transmon $ g\rangle$ - $ f\rangle$ shift	$\chi_b^f/2\pi$	9.76 MHz
Cavity b anharmonicity	$K_{bb}/2\pi$	71 kHz (81 kHz [†])
Cavity b T_1	T_{1b}	216 μ s
Cavity b T_2	T_{2b}	200 μ s
Cavity b $ 1\rangle_b$ population		$\sim 1\%$
Cavity a - b cross-Kerr	$K_{ab}/2\pi$	48 kHz (53 kHz [†])
Cavity a - r cross-Kerr	$K_{ar}/2\pi$	7 kHz
Cavity b - r cross-Kerr	$K_{br}/2\pi$	58 kHz

[†] Values measured in the presence of the relatively strong four-wave mixing tone.

* K_{aa} is estimated from the measured K_{ab} and K_{bb} .

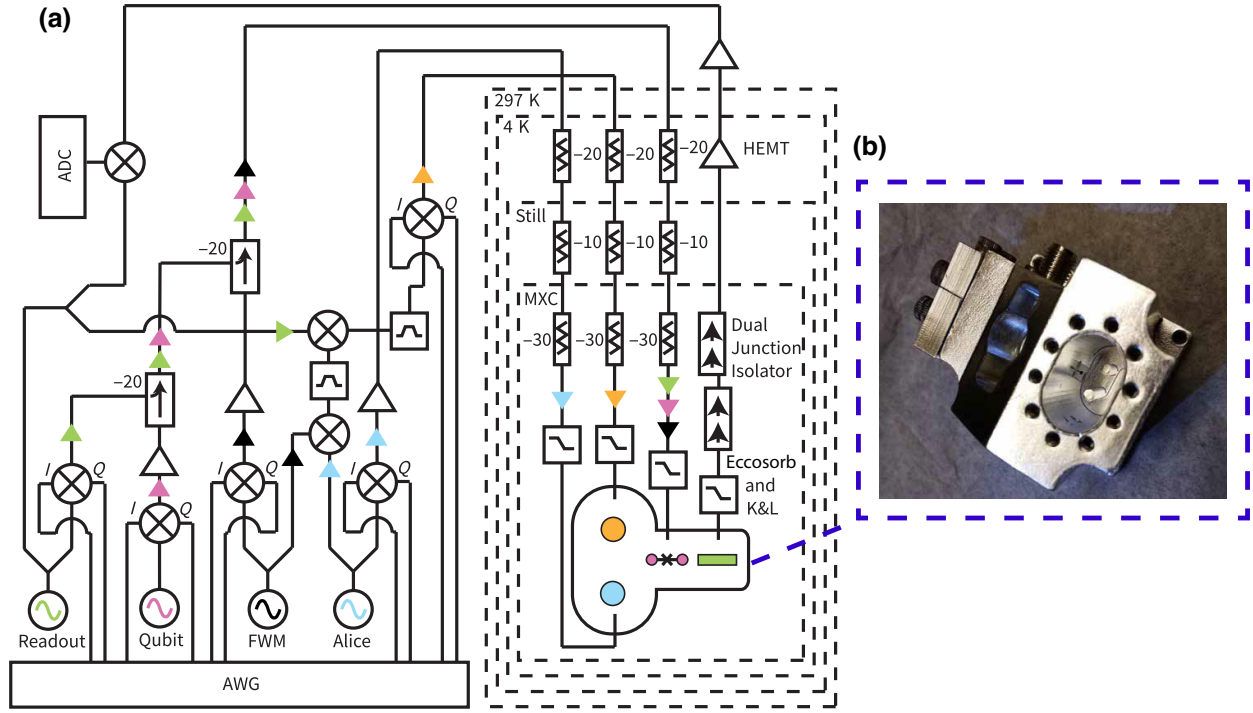


FIG. 7. (a) The refrigerator and measurement wiring diagram. We have four signal generators which, with eight AWG channels, make input signals for all the modes and FWM tone. The measurement setup shows that the drive signal for cavity b is generated by mixing the signals from cavity a , the reservoir, and the FWM generators with three-port mixers and using the correct sideband filters. (b) The high-purity aluminum cavity used in the experiment. The posts that give the storage-cavity modes are seen inside the aluminum body, with the sapphire chip entering the cavity from a side tunnel. The chip is held by an aluminum clamp and the transmon-qubit antenna is at equal distance from both of the posts. The cavity is mounted on a bracket that is placed inside a high-permeability magnetic shield thermalized to the mixing chamber.

smearing out any phase coherence. We therefore eliminate a phase degree of freedom by generating cavity b drive from a reservoir, cavity a , and the four-wave mixing generators. As shown in Fig. 7(a), the signal from the generators for the four-wave mixing pump and the cavity a drive are mixed with a three-port mixer which, with a low-pass filter, produces an output signal at $\omega_a - \omega_p$. This signal is again mixed with the signal from the reservoir-drive generator with a three-port mixer and a low-pass filter on the output to produce $\omega_r - \omega_a + \omega_p$, thus generating a local oscillator for the IQ mixer, modulating the sideband for driving cavity b .

3. Pump tuneup procedure

Given the presence of the storage-reservoir cross-Kerr interaction, there is no perfect experimental pumping condition that can exactly stabilize the PCS. In our experimental procedure, with the intention of studying driven dissipative dynamics, we aim to maximize the pair-photon dissipation rate κ_{ab} while empirically obtaining a steady state with relatively large photon numbers and minimal undesirable heating effects.

In order to maximize the ratio of the two-photon dissipation rate to the single-photon loss rate in the cavities $\kappa_{ab}/\kappa_{a,b}$, a relatively strong FWM pump amplitude g_{ab} is needed. We set the power of the FWM pump at a value at which we start to observe a small measurable rise of the excited state population of the ancilla transmon. The power of the reservoir drive is set to displace the reservoir to a few photons in its steady state, as can be measured via the Stark shift and dephasing of the transmon. We start by setting the frequency of the reservoir and FWM drive to be on resonance with the reservoir ω_r and the FWM condition $\omega_p = \omega_a + \omega_b - \omega_r$, respectively. We also use spectroscopy measurements to calibrate the Stark-shifted mode frequencies, which give us improved estimates of the pumping frequency condition. These two crudely set tones allow preparation of some nontrivial pair-photon states (e.g., with substantial $|11\rangle$ and $|22\rangle$ states) after 10–20 μ s of pumping time.

To calibrate the optimal frequency for the FWM pump that maximizes κ_{ab} , we start with the above crudely prepared state and then attempt to apply only the mixing pump at varying frequencies to evacuate photons in pairs. We finely sweep through the FWM frequencies and measure the population of $|00\rangle$ after a fixed amount of pumping

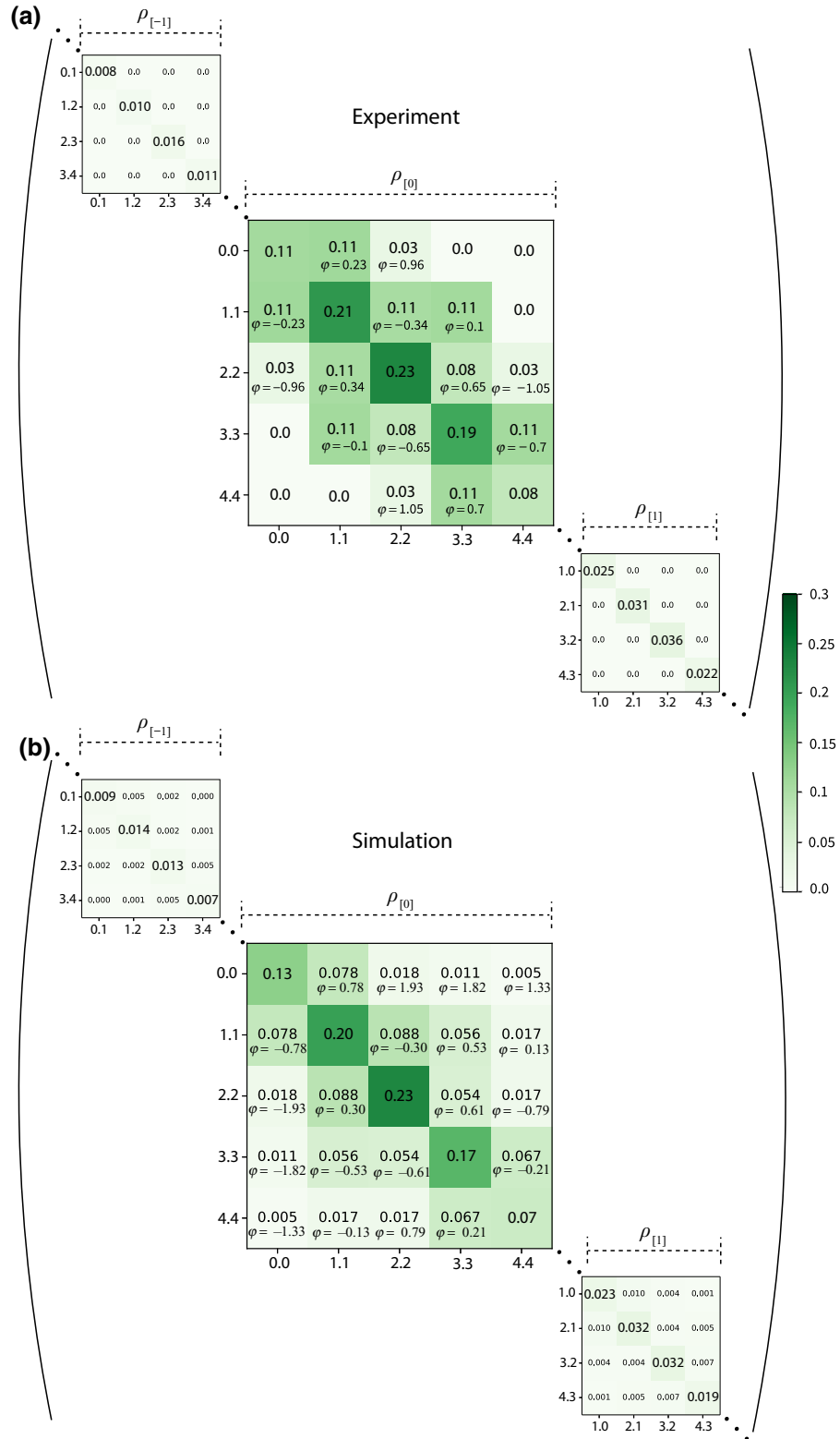


FIG. 8. The density matrix from experiment versus the simulation. (a) The experimental density matrix ρ_M measured using the quantum subspace-tomography method discussed in the main text for $d = 2$ after pumping for $t = 15 \mu\text{s}$ and with a wait time of $t_w = 4.5 \mu\text{s}$. (b) The simulated density matrix with the system parameters in Table II and rates extracted from the time-domain data fits as in Fig. 2, with the same t and t_w .

time. The FWM detuning Δ_p at which we get the largest $|00\rangle$ state gives the maximum κ_{ab} . Experimentally, we find $\Delta_p = -125$ kHz relative to the expected value from undriven mode frequencies $\omega_p = \omega_a + \omega_b - \omega_r$, primarily due to the Stark shift. We can extract the two-photon dissipation rate κ_{ab} from these decay measurements by fitting them to simulations as discussed in Appendix C.

The next step is to tune the amplitude and frequency of the reservoir drive to make a relatively large $\delta = 0$ pair-photon state with a Poisson-like distribution of Fock-state amplitudes in line with the PCS distribution. We find that the optimal reservoir-drive frequency is about -185 kHz detuned from its bare frequency, which can be explained by the cross-Kerr effect \hat{H}_{rk} in the presence of storage photons and the ac Stark effect from the pump tone. Finally, in a verification experiment depicted in Fig. 2(b), we measure the cavity-photon population distribution after $15 \mu\text{s}$ of stabilization drives with a fixed reservoir-drive condition while varying the FWM frequency. This figure shows that indeed the pair-photon drive is also most efficient when we pump at the FWM frequency tuned up to the previously determined Δ_p based on maximizing pair-photon dissipation.

4. Readout

We perform a dispersive readout by measuring the complex transmission coefficient from the reservoir mode that we interpret as a point in the IQ plane. This is done by preparing the qubit in the two states to be distinguished (either $|g\rangle$ - $|e\rangle$ or $|e\rangle$ - $|f\rangle$, where $|g\rangle$ is just an equilibrium state reached after sufficient wait time; thus it includes a small amount of thermal excitations) and then performing a transmission measurement through the readout cavity to determine the IQ point and repeating this process with sufficient averaging. These two points are used to define a projective axis that can be normalized such that the point along this axis can be interpreted as the probability of the qubit state. Our readout is placed at the reservoir frequency corresponding to the qubit in $|e\rangle$ because this yields good distinguishability for both $|g\rangle$ - $|e\rangle$ and $|e\rangle$ - $|f\rangle$ for our experimental parameter regime of $\chi_r > \kappa$. Our measurement efficiency is low due to the lack of a first-stage parametric amplifier before the 4-K stage and additional technical noise. As a result, our readout pulse has a relatively long duration length of $6 \mu\text{s}$, chosen to balance the qubit relaxation error and the signal-to-noise ratio.

For spectroscopy measurements, as in Figs. 2 and 3, the measured spectrum is fitted to a sum of Gaussian peaks (since the qubit pulse is Gaussian) with a background offset value. The sum of the Gaussian peaks is then used to renormalize the data to take into account experimental imperfections (namely, incomplete rotations). The heights of these normalized Gaussian peaks, which are roughly (not exact due to higher-order nonlinearities) at frequency

$-n\chi_a - m\chi_b$, can then be interpreted as the population of the $|nm\rangle$ state. Due to noise and imperfect calibration of offset and peak height parameters in our fittings along with small phase drifts, these fluctuations can lead to small unphysical negative values, as seen in the spectroscopy measurements.

Subspace-tomography measurements are, in essence, spectroscopy measurements of the $|e\rangle$ - $|f\rangle$ transition for selected components of the quantum state that have been placed in the $|e\rangle$ manifold. In these tomographic measurements, the $|f\rangle$ state probability from the readout is normalized by the sum of the two Gaussian peaks in the same $|e\rangle$ - $|f\rangle$ spectroscopy without tomographic displacement pluses. This normalization yields the relative fraction of population within the subspace S (as plotted in Fig. 5) in a self-calibrated manner, which is then used to compute the relative coherence between the original two Fock components.

For Wigner-tomography measurements, to symmetrize systematic bias caused by transmon decoherence, each data point is computed from the difference between two measurements where the mapping of joint parity of the storage modes and the qubit state is even (odd) $\rightarrow |e\rangle (|f\rangle)$ and even (odd) $\rightarrow |f\rangle (|e\rangle)$ for the first and second runs, respectively, thus mapping the values to the parity scale between 1 and -1 .

APPENDIX B: DRIVEN HAMILTONIAN AND ADIABATIC ELIMINATION

1. Rotating-frame Hamiltonian transformation

In this appendix, we derive the four-wave mixing effect of the off-resonant pump tone on the Josephson circuit under the rotating-wave approximation, arriving at the drive Hamiltonian in the rotating-frame equation [see Eq. (7)]. This procedure is similar to various previous experiments [29,32,55].

We start by writing our Hamiltonian as a sum of our four modes (reservoir, r ; qubit, q ; storage a , a ; storage b , b) coupled to a Josephson junction with two drives (FWM pump, p ; reservoir drive, d) applied to the reservoir mode [5]:

$$\hat{H}_{\text{full}}/\hbar = \sum_{m=q,r,a,b} \bar{\omega}_m \hat{m}^\dagger \hat{m} - E_J (\cos(\hat{\phi}) + \hat{\phi}^2/2) + 2\text{Re}(\epsilon_p e^{-i\omega_p t} + \epsilon_d e^{-i\omega_d t})(\hat{r} + \hat{r}^\dagger) \quad (\text{B1})$$

$$\hat{\phi} = \sum_{m=q,r,a,b} \phi_m (\hat{m}^\dagger + \hat{m}). \quad (\text{B2})$$

The first term in Eq. (B1) represents the linear character of each mode corresponding to a_i . The Josephson junction is represented by the cosine term, with E_J as the Josephson

energy and $\hat{\phi}$ as the phase across the junction, decomposed into the contributions from each mode with the contribution of ϕ_m to the zero-point fluctuations of $\hat{\phi}$. The two drive terms are acting on the reservoir mode with complex amplitudes ϵ_d and ϵ_p and frequencies ω_d and ω_p , respectively, where the pump is a strong off-resonant tone and the drive is a weak near-resonant tone with the reservoir mode.

We are in a regime where the following inequality holds:

$$\omega_p, \omega_d, \bar{\omega}_m \gg \epsilon_p \gg \frac{E_J}{\hbar} \|\hat{\phi}\|^4/4!. \quad (\text{B3})$$

We now want to make a change of frame using the following unitary to eliminate the fastest time scales:

$$U = e^{i\bar{\omega}_q \hat{q}^\dagger \hat{q}} e^{i\omega_d \hat{r}^\dagger \hat{r}} e^{i\omega_{da} \hat{a}^\dagger \hat{a}} e^{i\omega_{db} \hat{b}^\dagger \hat{b}} e^{-\tilde{\xi}_p \hat{r}^\dagger + \tilde{\xi}_p^* \hat{r}}. \quad (\text{B4})$$

We are rotating out the qubit frequency $\bar{\omega}_q$ simply for convenience, as it does not change the rest of the analysis in any meaningful way. We then rotate out the drive frequency ω_d on the reservoir mode so that the drive term is stationary in the chosen frame. We then want to put our storage modes in the drive frame of $\omega_d + \omega_p$. We can do this by rotating out frequency $\omega_{da}(\omega_{db})$ from mode $a(b)$. Any ω_{da}, ω_{db} that satisfy $\omega_{da} + \omega_{db} = \omega_d + \omega_p$ puts us in the correct drive frame; thus there is some freedom as to which frequencies we choose. Here, we choose a constant offset ($\Delta_{sd}/2$) of ω_{da}, ω_{db} from $\bar{\omega}_a, \bar{\omega}_b$, respectively, such that $\bar{\omega}_a - \omega_{da} = \bar{\omega}_b - \omega_{db} = \Delta_{sd}/2$. Finally, we want to apply a displacement unitary to eliminate the time-dependent amplitude ($\tilde{\xi}_p$) in the reservoir caused by the pump tone to bring the effect of this amplitude into the $\hat{\phi}$ operator, allowing the effects on the other modes to become directly apparent. Looking at times on the order or greater than $1/\kappa_r$, we can ignore the reservoir transient dynamics and look at the steady-state response of our displacement amplitude, as done in Ref. [29]:

$$\begin{aligned} \tilde{\xi}_p &= \xi_p e^{-i\omega_p t}, \\ \xi_p &= \frac{-i\epsilon_p}{\kappa_r/2 + i(\bar{\omega}_r - \omega_p)} \approx \frac{-i\epsilon_p}{\kappa_r/2 + i(\omega_r - \omega_p)}. \end{aligned} \quad (\text{B5})$$

The Hamiltonian in this new frame (\hat{H}'_{full}) now becomes

$$\begin{aligned} \hat{H}'_{\text{full}}/\hbar &= (\bar{\omega}_r - \omega_d) \hat{r}^\dagger \hat{r} + \Delta_{sd} \hat{a}^\dagger \hat{a} \\ &+ \Delta_{sd} \hat{b}^\dagger \hat{b} - \frac{E_J}{\hbar} (\cos(\tilde{\phi}) + \tilde{\phi}^2/2), \end{aligned} \quad (\text{B6})$$

$$\tilde{\phi} = \sum_{m=q,r,a,b} \phi_m (\tilde{m} + \tilde{m}^\dagger) + (\tilde{\xi}_p + \tilde{\xi}_p^*) \phi_r, \quad (\text{B7})$$

$$\begin{aligned} \tilde{q} &= \hat{q} e^{-i\bar{\omega}_q t}, \tilde{r} = \hat{r} e^{-i\omega_d t}, \\ \tilde{a} &= \hat{a} e^{-i\omega_{da} t}, \tilde{b} = \hat{b} e^{-i\omega_{db} t}. \end{aligned} \quad (\text{B8})$$

We now expand the cosine term to fourth order, keep only nonrotating terms in alignment with the rotating-wave approximation, and separate the Hamiltonian into three parts ($\hat{H}'_{\text{full}} = \hat{H}_{\text{freq}} + \hat{H}_{\text{Kerr}} + \hat{H}_{\text{drive}}$) as defined below:

$$\begin{aligned} \hat{H}_{\text{freq}} &= (-\chi_{qr} |\xi_p|^2) \hat{q}^\dagger \hat{q} \\ &+ (\omega_r - \omega_d - 2K_{rr} |\xi_p|^2) \hat{r}^\dagger \hat{r} \\ &+ (\Delta_{sd} - K_{ar} |\xi_p|^2) \hat{a}^\dagger \hat{a} \\ &+ (\Delta_{sd} - K_{br} |\xi_p|^2) \hat{b}^\dagger \hat{b}, \end{aligned} \quad (\text{B9})$$

$$\begin{aligned} \hat{H}_{\text{Kerr}} &= \sum_{m=r,a,b} -\frac{K_{mm}}{2} (\hat{m}^\dagger \hat{m})^2 - \alpha_q (\hat{q}^\dagger \hat{q})^2 - \chi_{qr} \hat{q}^\dagger \hat{q} \hat{r}^\dagger \hat{r} \\ &- K_{ar} \hat{a}^\dagger \hat{a} \hat{r}^\dagger \hat{r} - K_{br} \hat{b}^\dagger \hat{b} \hat{r}^\dagger \hat{r} - K_{ab} \hat{b}^\dagger \hat{b} \hat{a}^\dagger \hat{a} \end{aligned} \quad (\text{B10})$$

$$\hat{H}_{\text{int}} = g_{ab} \hat{a}^\dagger \hat{b}^\dagger \hat{r} + \epsilon_d \hat{r}^\dagger + \text{h.c.} \quad (\text{B11})$$

H_{freq} gives the frequency shifts to all the elements and the shifts from terms containing $|\xi_p|^2$ are the ac Stark shift effects from the pump tone. H_{Kerr} corresponds to both the self- and cross-Kerr coupling terms, where $K_{mm} = E_J/(\hbar) \phi_m^4/2$ and $K_{mm'} = E_J/(\hbar) \phi_m^2 \phi_{m'}^2$, in which $m \neq m'$ and $g_{ab} = \phi_a \phi_b \phi_r^2 \xi_p$. Note that H_0 in Eq. (3) is analogous to H_{Kerr} with just a truncation of the allowed qubit states to the $|f\rangle$ state.

2. Semiclassical analysis of reservoir state

In this section, we perform a semiclassical analysis of the Langevin equations of motion for the reservoir and storage modes and show that the impact of the storage states on the reservoir dynamics is quite small and warrants treating the effect as a small perturbation. This condition forms the basis for the adiabatic elimination of the reservoir mode in Appendix B 3.

We first assume that the qubit is in the ground state during the stabilization. This leads us to work with the Hamiltonian:

$$\begin{aligned} \hat{H} &= \Delta_d \hat{r}^\dagger \hat{r} + \Delta_a \hat{a}^\dagger \hat{a} + \Delta_b \hat{b}^\dagger \hat{b} \\ &- \sum_{m=r,a,b} \frac{K_{mm}}{2} (\hat{m}^\dagger \hat{m})^2 - K_{ab} \hat{a}^\dagger \hat{a} \hat{b}^\dagger \hat{b} \\ &- K_{ar} \hat{a}^\dagger \hat{a} \hat{r}^\dagger \hat{r} - K_{br} \hat{b}^\dagger \hat{b} \hat{r}^\dagger \hat{r} + \hat{H}_{\text{int}}, \end{aligned} \quad (\text{B12})$$

where $\Delta_d = (\omega_r - \omega_d - 2K_{rr} |\xi_p|^2)$, $\Delta_a = (\Delta_{sd} - K_{ar} |\xi_p|^2)$, $\Delta_b = (\Delta_{sd} - K_{br} |\xi_p|^2)$. For simplicity, in the following analysis we focus on analyzing the $\delta = 0$ storage

state but the conclusion, as is explained later, is general. In this state, our $\hat{a}^\dagger \hat{a}$ and $\hat{b}^\dagger \hat{b}$ terms are equivalent; thus we can group the storage-cavity self- and cross-Kerr terms into one Kerr term, $K_{\text{eff}} \hat{a}^\dagger \hat{a} \hat{b}^\dagger \hat{b}$, where $K_{\text{eff}} = -K_{ab} - K_{aa}/2 - K_{bb}/2$. This yields the following simplified Hamiltonian ($\hat{H}_{\delta 0}$) for a $\delta = 0$ state:

$$\begin{aligned} \hat{H}_{\delta 0} = & \Delta_d \hat{r}^\dagger \hat{r} + \Delta_a \hat{a}^\dagger \hat{a} + \Delta_b \hat{b}^\dagger \hat{b} \\ & - \frac{K_{rr}}{2} (\hat{r}^\dagger \hat{r})^2 + K_{\text{eff}} \hat{a}^\dagger \hat{a} \hat{b}^\dagger \hat{b} \\ & - K_{ar} \hat{a}^\dagger \hat{a} \hat{r}^\dagger \hat{r} - K_{br} \hat{a}^\dagger \hat{a} \hat{r}^\dagger \hat{r} + \hat{H}_{\text{int}}. \end{aligned} \quad (\text{B13})$$

We now want to motivate the statement that the effect of the storage modes on the reservoir is quite small compared to both the effects of the pumping (g_{ab}) and the reservoir-storage cross-Kerr (K_{ar}, K_{br}). The pumping effects can be seen by looking at the Langevin equations for the classical amplitude analogs of $\langle \hat{r} \rangle \rightarrow r$ and $\sqrt{\langle \hat{a} \hat{b} \rangle} \rightarrow s$ in this Hamiltonian. We can then obtain the steady-state solutions to these Langevin equations:

$$\begin{aligned} \frac{d}{dt} r &= -i\epsilon_d - (\kappa_r/2 + i\Delta_d)r - ig_{ab}^* s^2 = 0, \\ \frac{d}{dt} s &= -2ig_{ab} s^* r + 2iK_{\text{eff}} |s|^2 s = 0. \end{aligned} \quad (\text{B14})$$

From this, we can solve algebraically for the steady-state mode amplitude:

$$r = \frac{\epsilon_d}{-\frac{|g_{ab}|^2}{K_{\text{eff}}} + \frac{i(\kappa_r + 2i\Delta_d)}{2}}. \quad (\text{B15})$$

We are in the limit of $|\kappa_r + 2i\Delta_d| \gg 2|g_{ab}|^2/K_{\text{eff}}$, so we can look at the mode amplitude as an uncoupled driven mode with a perturbation from the coupling to the storage cavity as

$$\begin{aligned} r &\approx r_0 + \delta_{\text{disp}}, \\ r_0 &= \frac{2\epsilon_d}{i(\kappa_r + 2i\Delta_d)}, \\ \delta_{\text{disp}} &= -\frac{4\epsilon_d |g_{ab}|^2}{K_{\text{eff}}(\kappa_r + 2i\Delta_d)^2} \cdot |\delta_{\text{disp}}| \ll 1 \end{aligned} \quad (\text{B16})$$

For our experimental parameters, $|r_0| = 1.8$. We note that the storage-reservoir Langevin equation Eq. (B14) takes a similar form as in previous single-mode two-photon driven-dissipation experiments [29,31] but our system is in a different parameter regime due to the presence of a large K_{eff} . In the absence of K_{eff} , the steady-state r would be close to 0 even if $|r_0| > 1$.

While this is derived under the steady state and with a $\delta = 0$ state to more concretely illustrate the point, one

can more generally consider the “pull” that the storage modes have on the reservoir as $|g_{ab}|^2/K_{\text{eff}}$, compare this to the loss rate κ_r , and see that we are in a regime where $\kappa_r \gg |g_{ab}|^2/K_{\text{eff}}$; thus the effect of the storage modes on the reservoir state via the pumping effects is quite small. Now, the storage-reservoir cross Kerr effects must be taken into account. The cross-Kerr values will simply add a further detuning on top of Δ_d to the reservoir amplitude for each number state of the storage. Since our pair-coherent-state amplitude γ is on the order of the photon number in each mode in the system for the $\delta = 0$ state that we are analyzing, we use this to represent the average photon number in the inequality. Thus, we must satisfy the inequality $\kappa_r \gg \gamma(K_{ar} + K_{br})$ to ensure that the effects of the storage-reservoir cross Kerr can be treated as a perturbation on top of the bare reservoir amplitude. Since our parameter regime satisfies $\kappa_r \gg \gamma(K_{ar} + K_{br})$, $|g_{ab}|^2/K_{\text{eff}}$, we are well motivated to treat the reservoir amplitude as an uncoupled amplitude r_0 with a perturbation added to account for the effect from the storage modes.

3. Adiabatic elimination of the reservoir mode

In this section, we use the above analysis of the reservoir dynamics as an uncoupled amplitude with a small perturbation accounting for the storage mode effects to adiabatically eliminate the reservoir mode. We do this by going into a displaced frame of the reservoir mode using the uncoupled mode amplitude r_0 , in which the resulting reservoir state is solely from the perturbation effects of the storage mode and hence remains close to vacuum. This small resulting reservoir amplitude allows us to write the density matrix as a perturbative expansion in the reservoir states. Then, using the fast time scale of κ_r , we can adiabatically eliminate the reservoir mode, to arrive at Eq. (8).

Using the above analysis of the reservoir mode, we can apply a unitary transformation $U_{\text{disp}} = e^{-r_0 \hat{r}^\dagger + r_0^* \hat{r}}$ to \hat{H} , resulting in $\hat{H}' = U_{\text{disp}} \hat{H} U_{\text{disp}}^\dagger$, to go into a frame where the coherent state displacement on the reservoir mode is represented by just δ_{disp} in addition to the effect on the amplitude from the reservoir-storage cross-Kerr effects, which are also small:

$$\begin{aligned} \hat{H}' = & \Delta_d (\hat{r}^\dagger \hat{r} + \hat{r}^\dagger r_0 + \hat{r} r_0^* + |r_0|^2) + \Delta_a \hat{a}^\dagger \hat{a} \\ & + \Delta_b \hat{b}^\dagger \hat{b} - \sum_{m=r,a,b} \frac{K_{mm}}{2} (\hat{m}^\dagger \hat{m})^2 - K_{ab} \hat{a}^\dagger \hat{a} \hat{b}^\dagger \hat{b} \\ & - (K_{ar} \hat{a}^\dagger \hat{a} + K_{br} \hat{b}^\dagger \hat{b}) (\hat{r}^\dagger \hat{r} + \hat{r}^\dagger r_0 + \hat{r} r_0^* + |r_0|^2) \\ & + g_{ab} \hat{a}^\dagger \hat{b}^\dagger (\hat{r} + r_0) + \epsilon_d (\hat{r}^\dagger + r_0^*) \\ & + g_{ab}^* \hat{a} \hat{b} (\hat{r} + r_0) + \epsilon_d^* (\hat{r} + r_0). \end{aligned} \quad (\text{B17})$$

We can first omit all constant-energy offset terms and then combine the $\Delta_d r_0 \hat{r}^\dagger + \text{h.c.}$ terms with the resulting

κ_r Lindbladian loss-operator terms of the same order from the same unitary transformation to cancel out the ϵ_d terms, yielding the following simplified \hat{H}' :

$$\begin{aligned}\hat{H}' = & \Delta_d \hat{r}^\dagger \hat{r} + \Delta_a \hat{a}^\dagger \hat{a} + \Delta_b \hat{b}^\dagger \hat{b} \\ & - \sum_{m=r,a,b} \frac{K_{mm}}{2} (\hat{m}^\dagger \hat{m})^2 - K_{ab} \hat{a}^\dagger \hat{a} \hat{b}^\dagger \hat{b} \\ & - (K_{ar} \hat{a}^\dagger \hat{a} + K_{br} \hat{b}^\dagger \hat{b}) (\hat{r}^\dagger \hat{r} + \hat{r}^\dagger r_0 + \hat{r} r_0^* + |r_0|^2) \\ & + g_{ab} \hat{a}^\dagger \hat{b}^\dagger (\hat{r} + r_0) + g_{ab}^* \hat{a} \hat{b} (\hat{r}^\dagger + r_0^*). \quad (\text{B18})\end{aligned}$$

Now, we can group terms that are small and say that the dimensionless quantities $(\gamma(K_{ar} + K_{br}))/\kappa_r$, δ_{disp} , $\kappa_{a(b)}/\kappa_r$, g_{ab}/κ_r , and $K_{aa(bb)}/\kappa_r$ are on the order of ϵ , where $\epsilon \ll 1$ and $r_0 \approx \mathcal{O}(1)$. Since, as explained earlier, our reservoir state size is small, $\mathcal{O}(\epsilon)$, in this displaced frame, to a good approximation we can decompose our full density matrix with both storage modes and the reservoir (ρ_{abr}) as follows, where ρ_{ij} signifies the reduced density-matrix element of the storage cavities alone entangled with the reservoir state $|i\rangle \langle j|$:

$$\begin{aligned}\rho_{\text{abr}} = & \rho_{00} |0\rangle \langle 0| + \epsilon(\rho_{01} |0\rangle \langle 1| + \rho_{10} |1\rangle \langle 0|) \\ & + \epsilon^2(\rho_{11} |1\rangle \langle 1| + \rho_{02} |0\rangle \langle 2| + \rho_{20} |2\rangle \langle 0|). \quad (\text{B19})\end{aligned}$$

We now take $\Delta_d = (\Delta_a - K_{ar}|r_0|^2) = (\Delta_b - K_{br}|r_0|^2) = 0$ because, experimentally, we drive the reservoir on resonance after the Stark shift is accounted for and we calibrate our drives such that $2\Delta_{sd} = K_{ar}|r_0|^2 + K_{br}|r_0|^2 + K_{ar}|\xi_p|^2 + K_{br}|\xi_p|^2$. For a $\delta = 0$ state: this calibrated equality is analogous to setting $(\Delta_a - K_{ar}|r_0|^2) = (\Delta_b - K_{br}|r_0|^2) = 0$. This brings us to the following master equation for our density matrix ρ_{abr} :

$$\begin{aligned}\frac{d}{dt} \rho_{\text{abr}} = & -i[\hat{H}', \rho_{\text{abr}}] + \kappa_r D[\hat{r}] \rho_{\text{abr}} \\ & + \kappa_a D[\hat{a}] \rho_{\text{abr}} + \kappa_b D[\hat{b}] \rho_{\text{abr}}. \quad (\text{B20})\end{aligned}$$

We can now use this to derive the dynamics of just the storage cavities (ρ) from obtaining $\text{Tr}_r[\rho_{\text{abr}}] = \rho_{00} + \epsilon^2 \rho_{11}$ up to second order in ϵ . First, looking at the evolution of ρ_{00} by multiplying our master equation by $\langle 0|$ and $|0\rangle$, we obtain

$$\begin{aligned}\frac{1}{\kappa_r} \frac{d}{dt} \rho_{00} = & -\frac{i}{\kappa_r} \langle 0| [\hat{H}', \rho_{\text{abr}}] |0\rangle + \epsilon^2 \rho_{11} \\ & + \frac{\kappa_a}{\kappa_r} D[\hat{a}] \rho_{00} + \frac{\kappa_b}{\kappa_r} D[\hat{b}] \rho_{00}\end{aligned}$$

$$\begin{aligned}= & -i\epsilon^2 (\hat{A}^\dagger \rho_{10} - \rho_{01} \hat{A}) \\ & - i \left[-\frac{K_{aa}}{2\kappa_r} (\hat{a}^\dagger \hat{a})^2 - \frac{K_{bb}}{2\kappa_r} (\hat{b}^\dagger \hat{b})^2 - \frac{K_{ab}}{\kappa_r} \hat{a}^\dagger \hat{a} \hat{b}^\dagger \hat{b} \right. \\ & \left. + \frac{g_{ab}}{\kappa_r} \hat{a}^\dagger \hat{b}^\dagger (r_0) + \frac{g_{ab}^*}{\kappa_r} \hat{a} \hat{b} (r_0^*), \rho_{00} \right] \\ & + \epsilon^2 \rho_{11} + \frac{\kappa_a}{\kappa_r} D[\hat{a}] \rho_{00} + \frac{\kappa_b}{\kappa_r} D[\hat{b}] \rho_{00}, \quad (\text{B21})\end{aligned}$$

where $A \equiv 1/\epsilon \kappa_r (g_{ab}^* \hat{a} \hat{b} - K_{ar} r_0 \hat{a}^\dagger \hat{a} - K_{br} r_0 \hat{b}^\dagger \hat{b})$, thus making $\|A\| \approx \mathcal{O}(1)$. Now, we can find similar evolution equations for ρ_{10} and ρ_{11} , working only up to zeroth order in ϵ :

$$\begin{aligned}\frac{1}{\kappa_r} \frac{d}{dt} \rho_{10} = & -i\hat{A} \rho_{00} - \frac{1}{2} \rho_{10} + \mathcal{O}(\epsilon), \\ \frac{1}{\kappa_r} \frac{d}{dt} \rho_{11} = & -i(\hat{A} \rho_{01} - \rho_{01} \hat{A}^\dagger) - \rho_{11} + \mathcal{O}(\epsilon).\end{aligned} \quad (\text{B22})$$

Looking at the equation for ρ_{10} , we can see that the first term involving ρ_{00} is time dependent, making an exact solution difficult, but the time rate of change can be seen to be slow, on the order of ϵ , whereas the second term, which acts as a damping term, is of order unity. Since the effective driving term is slowly changing and the damping term is relatively much stronger, we can impose an adiabatic elimination and take ρ_{10} to be in its steady state. The same argument would apply to ρ_{11} , yielding

$$\begin{aligned}\rho_{10} = & -2i\hat{A} \rho_{00} + \mathcal{O}(\epsilon), \\ \rho_{11} = & -i(\hat{A} \rho_{01} - \rho_{01} \hat{A}^\dagger) + \mathcal{O}(\epsilon) = 4\hat{A} \rho_{00} \hat{A}^\dagger + \mathcal{O}(\epsilon).\end{aligned} \quad (\text{B23})$$

Substitution of the above expressions for ρ_{00} , ρ_{10} , and ρ_{01} into Eq. (B21) yields the following master equation:

$$\begin{aligned}\frac{d}{dt} \rho = & -i[\hat{H}_{\text{red}}, \rho] + \kappa_a D[\hat{a}] \rho + \kappa_b D[\hat{b}] \rho \\ & + D \left[\frac{2g_{ab}^*}{\sqrt{\kappa_r}} \hat{a} \hat{b} - \frac{2K_{ar} r_0}{\sqrt{\kappa_r}} \hat{a}^\dagger \hat{a} - \frac{2K_{br} r_0}{\sqrt{\kappa_r}} \hat{b}^\dagger \hat{b} \right] \rho,\end{aligned} \quad (\text{B24})$$

where

$$\begin{aligned}\hat{H}_{\text{red}} = & -\frac{K_{aa}}{2} (\hat{a}^\dagger \hat{a})^2 - \frac{K_{bb}}{2} (\hat{b}^\dagger \hat{b})^2 \\ & - K_{ab} \hat{a}^\dagger \hat{a} \hat{b}^\dagger \hat{b} + \epsilon_{ab} \hat{a}^\dagger \hat{b}^\dagger + \epsilon_{ab}^* \hat{a} \hat{b}\end{aligned} \quad (\text{B25})$$

$$\epsilon_{ab} = g_{ab} r_0, \quad \kappa_{ab} = \frac{4|g_{ab}|^2}{\kappa_r}. \quad (\text{B26})$$

4. Ideal steady-state PCS without reservoir cross-Kerr

In this section, we show that the ideal pair-photon driven-dissipation process, in the absence of spurious reservoir cross-Kerr and single-photon loss, stabilizes a PCS as discussed in Table I.

Starting from Eqs. (B24) and (B25), this ideal scenario results in the equation of motion

$$\dot{\rho} = -i(\hat{H}_{\text{ideal}}\rho - \rho\hat{H}_{\text{ideal}}^\dagger) + \kappa_{ab}\hat{a}\hat{b}\rho\hat{a}^\dagger\hat{b}^\dagger, \quad (\text{B27})$$

$$\hat{H}_{\text{ideal}} = \epsilon_{ab}^*\hat{a}\hat{b} + \epsilon_{ab}\hat{a}^\dagger\hat{b}^\dagger + K_{\text{eff}}\hat{a}^\dagger\hat{b}^\dagger\hat{a}\hat{b} - i\frac{\kappa_{ab}}{2}\hat{a}^\dagger\hat{b}^\dagger\hat{a}\hat{b}. \quad (\text{B28})$$

If the system is in a PCS, $|\gamma, \delta\rangle$, we can write the instantaneous density-matrix time evolution as

$$\begin{aligned} \dot{\rho} = & (\epsilon_{ab}^*\gamma - \epsilon_{ab}\gamma^* + i\kappa_{ab}|\gamma|^2)\rho \\ & + (\epsilon_{ab} + K_{\text{eff}}\gamma - i\frac{\kappa_{ab}}{2}\gamma)\hat{a}^\dagger\hat{b}^\dagger\rho \\ & - (\epsilon_{ab}^* + K_{\text{eff}}\gamma^* + i\frac{\kappa_{ab}}{2}\gamma^*)\rho\hat{a}\hat{b}. \end{aligned} \quad (\text{B29})$$

Setting the terms that distort ρ to 0 will give a steady-state solution that yields the following expression for the PCS state size γ :

$$\gamma = \frac{\epsilon_{ab}}{\frac{i\kappa_{ab}}{2} - K_{\text{eff}}}. \quad (\text{B30})$$

APPENDIX C: NUMERICAL SIMULATION METHODS

We numerically simulate the PCS stabilization with two-photon pumping and dissipation that compares well with the experiment. The data shown in Fig. 2(d) are a measurement of the storage-cavity population while pumping the PCS for variable time and the inset is measuring the population when only the FWM drive is on, causing two-photon dissipation to start in a PCS. The Hamiltonian used in the simulation to fit the two-photon pumping and dissipation is unitary transformed, so that the PCS is stationary in the drive frame. The reservoir mode is adiabatically eliminated, resulting in a reduced Hamiltonian used in the master equation [see Eq. (8)] in the main text. We rewrite the master equation with the single-photon loss operators for both the storage cavities:

$$\begin{aligned} \partial_t \rho = & -i[\hat{H}_{sk} + (\epsilon_{ab}\hat{a}^\dagger\hat{b}^\dagger + \text{h.c.}), \rho] \\ & + \mathcal{D}[\sqrt{\kappa_{ab}}\hat{a}\hat{b} + \zeta_a\hat{a}^\dagger\hat{a} + \zeta_b\hat{b}^\dagger\hat{b}]\rho \\ & + \mathcal{D}[\sqrt{\kappa_a}\hat{a}]\rho + \mathcal{D}[\sqrt{\kappa_b}\hat{b}]\rho, \end{aligned} \quad (\text{C1})$$

where \hat{H}_{sk} is defined in Eq. (5) and

$$\zeta_a = -\frac{2K_{ar}r_0}{\sqrt{\kappa_r}}, \zeta_b = -\frac{2K_{br}r_0}{\sqrt{\kappa_r}}.$$

The storage-cavity single-photon loss rates, $\kappa_a = 1/T_{1a}$ and $\kappa_b = 1/T_{1b}$, Kerr, and cross-Kerr values measured during pumping are listed in Table II. The complex parameter $r_0 = 2\epsilon_d/(i\kappa_r - 2\Delta_d)$, first defined in Eq. (B16), is the reservoir displacement. We displace the reservoir with $\epsilon_d/2\pi = 780$ kHz at a detuning $\Delta_d/2\pi = -185$ kHz which, with $\kappa_r/2\pi = 780$ kHz, results in $|r_0| = 1.8$.

Starting in a PCS $|\gamma, \delta = 0\rangle$ as shown in Fig. 2(c), we measure the population of states at different times t_w for which only the FWM tone is on [Fig. 2(d inset)]. In the absence of the reservoir drive, the FWM drive should only cause two-photon dissipation $\mathcal{D}[\sqrt{\kappa_{ab}}\hat{a}\hat{b}]$. Using Eq. (C1) with κ_{ab} as the only fit parameter and no drive term, $\epsilon_{ab} = 0$, the time scale for two-photon dissipation can be extracted. The dephasing rates $\zeta_a = \zeta_b = 0$, since there are no photons in the reservoir and thus there is no dephasing caused by the storage-reservoir cross-Kerr $K_{ar/br}$. In the second part, we fix the two-photon dissipation $\kappa_{ab}/2\pi = 12.5$ kHz and vary ϵ_{ab} . We estimate the dephasing rates from cavities a and b , $|\zeta_a|^2/2 = 2\pi \times 0.4$ kHz and $|\zeta_b|^2/2 = 2\pi \times 28$ kHz, respectively. We find the two-photon pumping rate to be $\epsilon_{ab}/2\pi = 99$ kHz. The oscillations in the pumping time-domain data are the result of the weak dissipation rate compared to K_{eff} . The simulation shows that with $K_{\text{eff}} \gg \kappa_{ab}$, the damping of the oscillation from two-photon dissipation alone should be slower than we see in the experiment and the state is predicted by the equation for γ as in Table I. The state is smaller, with more PCS-like distribution. However, the modified dissipation operator to include dephasing effects of the cross-Kerr as derived in Appendix B produces faster damping, mimicking the experimental PCS distribution and size.

Using the equation $\kappa_{ab}/2\pi = 4|g_{ab}|^2/\kappa_r = 12.5$ kHz, we find $g_{ab}/2\pi = 50$ kHz. The Stark shift that we measure on the qubit due to the strong cw tone is approximately 4.3 MHz, which makes the fourth-order FWM term in the cosine expansion $g_{ab}/2\pi = 60$ kHz. This value of g_{ab} estimates $\epsilon_{ab}/2\pi = 120$ kHz and $\kappa_{ab}/2\pi = 18.4$ kHz—which, to a good approximation, is in agreement with the simulation. With the extracted two-photon dissipation and pumping rates, we simulate the coherence and phases over time in a subspace of the state [see Figs. 6(b) and 6(c)].

APPENDIX D: GENERAL PROTOCOL OF SUBSPACE TOMOGRAPHY

Using a three-level ancilla, we may use the following protocol for quantum subspace tomography as depicted in Fig. 9:

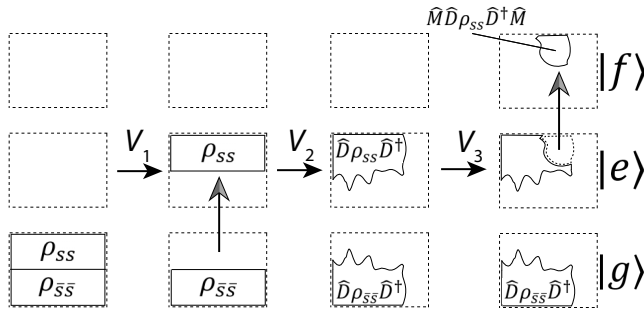


FIG. 9. The general protocol of subspace tomography. The occupied areas of the rectangles loosely depict nonzero regions of the cavity density matrices, where ρ_{ss} and $\rho_{\bar{s}\bar{s}}$ are blocks of the total-storage density matrix ρ . There are coherence elements between these two blocks that are not depicted because they do not impact the experiment at hand. The goal here is to isolate $\hat{M}\hat{D}\rho_{ss}\hat{D}^\dagger\hat{M}$ in the $|f\rangle$ subspace using the operations V_1 , V_2 , and V_3 , as shown in the image.

- (0) Start with the system-ancilla state $\rho \otimes |g\rangle\langle g|$.
- (1) Perform the unitary evolution $\hat{V}_1 = \exp[-i(\pi)/(2)\hat{P} \otimes (|e\rangle\langle g| + |g\rangle\langle e|)]$, which transforms the full density matrix into $\rho_1 = \hat{V}_1(\rho \otimes |g\rangle\langle g|)\hat{V}_1^\dagger = \rho_{ss} \otimes |e\rangle\langle e| + (\dots)$, where the terms (\dots) do not contribute to $|e\rangle$ state population or later measurement.
- (2) Perform the unitary evolution that preserves the ancilla basis states, $\hat{V}_2 = \sum_{j=g,e,f} \hat{U}_j \otimes |j\rangle\langle j|$. For a bosonic system, we may just apply displacement operation $\hat{U}_e = \hat{D}$, which transforms the density matrix into $\rho_2 = \hat{V}_2\rho_1\hat{V}_2^\dagger = \hat{D}\rho_{ss}\hat{D}^\dagger \otimes |e\rangle\langle e| + (\dots)$.
- (3) Choose the readout projector operator \hat{M} (e.g., the photon-number state projection $|nn\rangle\langle nn|$) and perform the unitary evolution $\hat{V}_3 = \exp[-i(\pi)/(2)\hat{M} \otimes (|f\rangle\langle e| + |e\rangle\langle f|)]$. The density matrix becomes $\rho_3 = \hat{V}_3\rho_2\hat{V}_3^\dagger = \hat{M}\hat{D}\rho_{ss}\hat{D}^\dagger\hat{M} \otimes |f\rangle\langle f| + (\dots)$.
- (4) Measure the probability in $|f\rangle$ state, $\text{Tr}[\rho_3 |f\rangle\langle f|] = \text{Tr}[\hat{M}\hat{D}\rho_{ss}\hat{D}^\dagger\hat{M}]$, which is sufficient for subspace tomography.

In principle, a measurement of the ancilla after step 1 (postselect on $|e\rangle$) can be used to physically project the cavity state to ρ_{ss} for subsequent subspace tomography. However, this requires highly ideal measurement properties including high single-shot fidelity, quantum nondemolition on the ancilla, and no spurious back action on the cavity system. In comparison, in the above protocol, the only requirement on the measurement is some degree of distinguishing ability between $|e\rangle$ and $|f\rangle$. The measurement outcome can be scaled from calibrated readout

contrast between $|e\rangle$ and $|f\rangle$ and any spurious readout signal from $|g\rangle$ only contributes to a background independent of \hat{D} and \hat{M} .

APPENDIX E: FREQUENCY MATCHING IN SUBSPACE TOMOGRAPHY

In a typical Ramsey-type experiment, one considers the rotating frame of a qubit or a cavity set by its first excitation pulse and the phases of its subsequent control pulses (usually at the same frequency) at any later time can be defined relative to the first pulse and programmed in the same rotating frame. In our subspace-tomography protocol, because individual pairwise coherence measurements involve ancilla rotation pulses of different frequencies, it is nontrivial to ensure that (1) the subspace-tomography pulse sequence carried out at any time (t or t_w) informs the superposition phase of cavity states consistently in a predefined frame and (2) the superposition phases of different Fock pairs are extracted consistently in the same rotating frame and hence can be combined in the same density matrix.

In our experiment, we enforce a “closed-loop” frequency-matching condition when choosing the frequency of the cavity displacement pulses (ω_3 and ω_4) in each of the 2D subspace-tomography measurements,

$$\omega_3 + \omega_4 = \omega_p + \omega_d - (\omega_1 - \omega_2), \quad (\text{E1})$$

where ω_p and ω_d are the stabilization drive frequencies. ω_1 and ω_2 are the frequencies of the photon-number-selective ancilla pulses and they must precisely match the dispersively shifted ancilla frequencies, with the dispersive shift

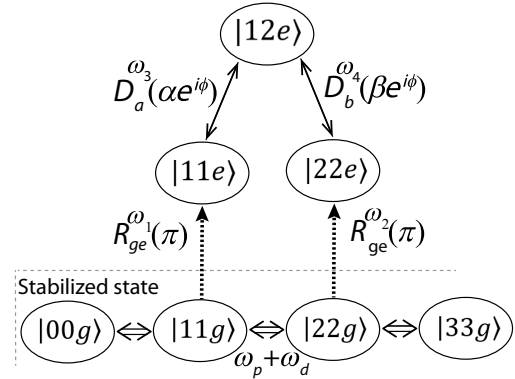


FIG. 10. A visual depiction of the pulse sequence used for the subspace tomography to determine the $\rho_{11,22}$ element while tracking the $|12\rangle$ state as a specific example. The frequencies of the four pulses applied in this tomographic analysis and the frequencies of the original cavity stabilization drives satisfy the “closed-loop” condition for phase locking: $\omega_1 - \omega_2 = \omega_p + \omega_d - \omega_3 - \omega_4$, which is the same effective equality as in Eq. (E5). Note that $\omega_1 - \omega_2 = \chi_{22} - \chi_{11} \approx \chi_{qa} + \chi_{qb}$ but is not exactly equal because of the sixth-order dispersive shifts.

being referred to as $-\chi_{jk}$ for the Fock state $|jk\rangle$ of the cavities. The closed loop in measuring the $|11\rangle$ - $|22\rangle$ interference as an example is illustrated in Fig. 10. While one could in principle account for accumulated phases from the relative timing and relative frequency difference of individual pulses without this condition, this strategy allows us to conveniently measure the two-cavity state in the “pump frame” defined by the two stabilization drives self-consistently. It is important to note that the main reason why it is important to satisfy this equality experimentally is that the dispersive shifts on the qubit due to different number states (χ_{jk}) are not equal to the corresponding multiples of χ_{qa} and χ_{qb} , i.e., $\chi_{jk} \neq j\chi_{qa} + k\chi_{qb}$, due to higher sixth-order terms in the cosine expansion of our Hamiltonian that have been neglected. Due to these neglected higher-order terms, ω_3 and ω_4 must be determined from the experimentally measured χ_{jk} values for each pair of number states to satisfy the equality.

In the following, we show how our subspace-tomography protocol faithfully extracts the superposition phase $\Phi_{jj} - \Phi_{kk}$ between two Fock components $|jj\rangle$ and $|kk\rangle$ of the cavity state as defined in the pump frame. (The analysis is easily extensible to $\delta \neq 0$ states.) In this analysis, we work in a rotating frame in which the transmon rotates with frequency ω_q and the two cavities rotate by a combined frequency $\omega_p + \omega_d$. (More specifically, cavity a rotates by $\omega_a - \Delta_{sd}/2$ and cavity b rotates by $\omega_b - \Delta_{sd}/2$ where $\Delta_{sd} = (\omega_a + \omega_b) - (\omega_p + \omega_d)$). In this rotating frame, the frequencies of the four tomography tones, $\omega_1, \omega_2, \omega_3$, and ω_4 are on the order of the dispersive shifts and the eigenfrequencies of the joint Fock states $|jj\rangle$ are

$$\omega_{jjg} = j\Delta_{sd} - K_{ab}j^2 - (K_{aa} + K_{bb})j(j-1)/2, \quad (\text{E2})$$

$$\omega_{jje} = j\Delta_{sd} - K_{ab}j^2 - (K_{aa} + K_{bb})j(j-1)/2 - \chi_{jj}, \quad (\text{E3})$$

for the transmons in $|g\rangle$ and $|e\rangle$, respectively.

We now track the phase accumulation on the $|jj\rangle$ component of the cavity state over the three time steps of a subspace tomography: first, the wait time (t_w a few microseconds after the PCS is made; next, the duration of our selective qubit pulse ($\delta t_q = 2 \mu\text{s}$) that excites it to be entangled with $|e\rangle$; and, finally, the duration of our displacement cavity pulses ($\delta t_d = 24 \text{ ns}$) to create interference of $|jje\rangle$ versus a different cavity state. The short duration and therefore the broad selectivity of our displacement cavity pulses gives us the freedom to vary their frequencies to satisfy this closed-loop condition without needing to worry about the frequencies being too far from the desired cavity states to be displaced. During the first wait-time period (t_w), the qubit remains in $|g\rangle$, thus accumulating a phase $\omega_{jjg}t_w$. During the qubit-pulse step (δt_q), the generator for the qubit pulse is rotating in a different

frame with a frequency offset of $-\chi_{jj}$, thus leading to a phase offset of $-\chi_{jj}(t_w + \delta t_q)$ from the phase imparted by the generator, since the generator would have been accumulating this phase through both time periods t_w and δt_q . We can use the same time steps here for different generators in different frames because they all share a common reference of how $t = 0$ is defined, where any reference point of $t = 0$ is valid provided that it is consistent among all generators. For our final time period, we have a state phase accumulation from the state with the qubit in $|e\rangle$ giving $\omega_{jje}\delta t_d$ in addition to the phase imparted by our displacement pulse. The displacement pulses are in different rotating frames with a combined frequency of $\omega_3 + \omega_4$. Taking the state that we are interfering with as $|kk\rangle$, this imparts a phase of $(\omega_3 + \omega_4)|k-j|(t_w + \delta t_q + \delta t_d)$, where the $|k-j|$ factor comes from the fact that the phase gets imparted for each excitation traded. With this, we can subtract the accumulated phases between $|jj\rangle$ and $|kk\rangle$ over the total time $t_{\text{tot}} = t_w + \delta t_q + \delta t_d$, where we are tracking state $|jj\rangle$ so that is the only one that will receive the $\omega_3 + \omega_4$ term. The state chosen to be tracked here does not matter, so this is still a general treatment, with the phase subtraction being

$$\begin{aligned} & \Phi_{jj} - \Phi_{kk} + (\omega_{jje} - \omega_{kke} + (\omega_3 + \omega_4)|k-j|)t_{\text{tot}} \\ &= \Phi_{jj} - \Phi_{kk} + (\omega_{jjg} - \omega_{kkq} + (\chi_{kk} - \chi_{jj} \\ &+ |k-j|(\omega_3 + \omega_4))t_{\text{tot}}. \end{aligned} \quad (\text{E4})$$

It is clear that we can simply calibrate our ω_3, ω_4 for each set of interference measurements on states $|jj\rangle$ and $|kk\rangle$ to satisfy the equality

$$\chi_{jj} - \chi_{kk} = |k-j|(\omega_3 + \omega_4), \quad (\text{E5})$$

so we can neglect a large part of Eq. (E4), leaving only $\Phi_{jj} - \Phi_{kk} + (\omega_{jjg} - \omega_{kkq})t_{\text{tot}}$. It is important to note that this cancellation we have imparted gets rid of any terms that could have contributions from higher-order neglected terms mentioned earlier and also allows an arbitrary choice of a consistent $t = 0$ definition across generators. This leaves us with the simple linear phase accumulation terms ω_{jjg} and ω_{kkq} that can be simply calculated and subtracted away, leaving the desired phase difference of $\Phi_{jj} - \Phi_{kk}$. This linear phase accumulation from $\omega_{jjg} - \omega_{kkq}$ can be seen for different states in Fig. 6(a) at different t_w values, allowing us to linearly extrapolate the original phase from the t_{tot} times.

One can think of this method in a more direct intuitive way by looking at the case of isolating $|11\rangle$ and $|22\rangle$ to determine the coherence element $\rho_{11,22}$ and seeing that on top of the desired $\Phi_{22} - \Phi_{11}$ and $(\omega_{22g} - \omega_{11g})t_{\text{tot}}$ phase contributions, there will be a constant phase accumulation over time with frequency of $-\chi_{22}$ and $-\chi_{11}$ on the $|11\rangle$ and $|22\rangle$ states, respectively. This is because while the cavity state $|11\rangle$ ($|22\rangle$) is entangled with the qubit in $|g\rangle$, the

generator that will send the pulse out to flip the state is rotating with a frequency of $-\chi_{11}(-\chi_{22})$, thus imparting the accumulated phase from this frequency difference, and after the rotation, there will be the same frequency difference due to the fact that the qubit is now in $|e\rangle$, so it will also rotate at a frequency of $-\chi_{11}(-\chi_{22})$ in this frame; so in effect this frequency accumulation will always be present. As mentioned earlier, there will additionally be the phase imparted from the displacement pulse, so we simply need to tune the ω_3 and ω_4 values to satisfy the above inequality in Eq. (E5) to cancel out the effects from the $-\chi_{11}, -\chi_{22}$ terms, thus leaving only the desired phase difference of $\Phi_{22} - \Phi_{11}$ and the linear phase accumulation from $\omega_{22g} - \omega_{11g}$, which can easily be subtracted away.

-
- [1] V. V. Dodonov, Nonclassical states in quantum optics: A review of the first 75 years, *J. Opt. B: Quantum Semiclass. Opt.* **4**, R1 (2002).
 - [2] S. L. Braunstein and P. van Loock, Quantum information with continuous variables, *Rev. Mod. Phys.* **77**, 513 (2005).
 - [3] A. Joshi, K. Noh, and Y. Y. Gao, Quantum information processing with bosonic qubits in circuit QED, *Quantum Sci. Technol.* **6**, 033001 (2021).
 - [4] W.-L. Ma, S. Puri, R. J. Schoelkopf, M. H. Devoret, S. M. Girvin, and L. Jiang, Quantum control of bosonic modes with superconducting circuits, *Sci. Bull.* **66**, 1789 (2021).
 - [5] A. Blais, A. L. Grimsmo, S. M. Girvin, and A. Wallraff, Circuit quantum electrodynamics, *arXiv:2005.12667* [quant-ph] (2020).
 - [6] B. Vlastakis, G. Kirchmair, Z. Leghtas, S. E. Nigg, L. Frunzio, S. M. Girvin, M. Mirrahimi, M. H. Devoret, and R. J. Schoelkopf, Deterministically encoding quantum information using 100-photon Schrödinger cat states, *Science* **342**, 607 (2013).
 - [7] C. Wang, Y. Y. Gao, P. Reinhold, R. W. Heeres, N. Ofek, K. Chou, C. Axline, M. Reagor, J. Blumoff, K. M. Sliwa, L. Frunzio, S. M. Girvin, L. Jiang, M. Mirrahimi, M. H. Devoret, and R. J. Schoelkopf, A Schrödinger cat living in two boxes, *Science* **352**, 1087 (2016).
 - [8] A. Grimm, N. E. Frattini, S. Puri, S. O. Mundhada, S. Touzard, M. Mirrahimi, S. M. Girvin, S. Shankar, and M. H. Devoret, Stabilization and operation of a Kerr-cat qubit, *Nature* **584**, 205 (2020).
 - [9] P. Campagne-Ibarcq, A. Eickbusch, S. Touzard, E. Zalys-Geller, N. E. Frattini, V. V. Sivak, P. Reinhold, S. Puri, S. Shankar, R. J. Schoelkopf, L. Frunzio, M. Mirrahimi, and M. H. Devoret, Quantum error correction of a qubit encoded in grid states of an oscillator, *Nature* **584**, 368 (2020).
 - [10] A. O. Barut and L. Girardello, New “coherent” states associated with non-compact groups, *Commun. Math. Phys.* **21**, 41 (1971).
 - [11] G. S. Agarwal, Generation of Pair Coherent States and Squeezing via the Competition of Four-Wave Mixing and Amplified Spontaneous Emission, *Phys. Rev. Lett.* **57**, 827 (1986).
 - [12] G. S. Agarwal and A. Biswas, Quantitative measures of entanglement in pair-coherent states, *J. Opt. B: Quantum Semiclass. Opt.* **7**, 350 (2005).
 - [13] M. S. Malcuit, D. J. Gauthier, and R. W. Boyd, Suppression of Amplified Spontaneous Emission by the Four-Wave Mixing Process, *Phys. Rev. Lett.* **55**, 1086 (1985).
 - [14] H. Zhang, A. Alsaedi, T. Hayat, and F.-G. Deng, Entanglement concentration and purification of two-mode squeezed microwave photons in circuit QED, *Ann. Phys. (New York)* **391**, 112 (2018).
 - [15] V. V. Albert, S. O. Mundhada, A. Grimm, S. Touzard, M. H. Devoret, and L. Jiang, Pair-cat codes: Autonomous error-correction with low-order nonlinearity, *Quantum Sci. Technol.* **4**, 035007 (2019).
 - [16] R. W. Heeres, P. Reinhold, N. Ofek, L. Frunzio, L. Jiang, M. H. Devoret, and R. J. Schoelkopf, Implementing a universal gate set on a logical qubit encoded in an oscillator, *Nat. Commun.* **8**, 1 (2017).
 - [17] Y. Y. Gao, B. J. Lester, K. S. Chou, L. Frunzio, M. H. Devoret, L. Jiang, S. M. Girvin, and R. J. Schoelkopf, Entanglement of bosonic modes through an engineered exchange interaction, *Nature* **566**, 509 (2019).
 - [18] S. Chakram, K. He, A. V. Dixit, A. E. Orian, R. K. Naik, N. Leung, H. Kwon, W.-L. Ma, L. Jiang, and D. I. Schuster, Multimode photon blockade, *Nat. Phys.* **18**, 879 (2022).
 - [19] N. Ofek, A. Petrenko, R. Heeres, P. Reinhold, Z. Leghtas, B. Vlastakis, Y. Liu, L. Frunzio, S. M. Girvin, L. Jiang, M. Mirrahimi, M. H. Devoret, and R. J. Schoelkopf, Extending the lifetime of a quantum bit with error correction in superconducting circuits, *Nature* **536**, 441 (2016).
 - [20] Y. Ma, Y. Xu, X. Mu, W. Cai, L. Hu, W. Wang, X. Pan, H. Wang, Y. P. Song, C.-L. Zou, and L. Sun, Error-transparent operations on a logical qubit protected by quantum error correction, *Nat. Phys.* **16**, 827 (2020).
 - [21] A. Essig, Q. Ficheux, T. Peronnin, N. Cottet, R. Lescanne, A. Sarlette, P. Rouchon, Z. Leghtas, and B. Huard, Multiplexed Photon Number Measurement, *Phys. Rev. X* **11**, 031045 (2021).
 - [22] J. F. Poyatos, J. I. Cirac, and P. Zoller, Quantum Reservoir Engineering with Laser Cooled Trapped Ions, *Phys. Rev. Lett.* **77**, 4728 (1996).
 - [23] D. Kienzler, H.-Y. Lo, B. Keitch, L. d. Clercq, F. Leupold, F. Lindenefelser, M. Marinelli, V. Negnevitsky, and J. P. Home, Quantum harmonic oscillator state synthesis by reservoir engineering, *Science* **347**, 53 (2015).
 - [24] M. Mirrahimi, Z. Leghtas, V. V. Albert, S. Touzard, R. J. Schoelkopf, L. Jiang, and M. H. Devoret, Dynamically protected cat-qubits: A new paradigm for universal quantum computation, *New. J. Phys.* **16**, 045014 (2014).
 - [25] J. Guillaud and M. Mirrahimi, Repetition Cat Qubits for Fault-Tolerant Quantum Computation, *Phys. Rev. X* **9**, 041053 (2019).
 - [26] S. Puri, L. St-Jean, J. A. Gross, A. Grimm, N. E. Frattini, P. S. Iyer, A. Krishna, S. Touzard, L. Jiang, A. Blais, S. T. Flammia, and S. M. Girvin, Bias-preserving gates with stabilized cat qubits, *Sci. Adv.* **6**, eaay5901 (2020).
 - [27] C. Chamberland, K. Noh, P. Arrangoiz-Arriola, E. T. Campbell, C. T. Hann, J. Iverson, H. Putterman, T. C.

- Bohdanowicz, S. T. Flammia, A. Keller, G. Refael, J. Preskill, L. Jiang, A. H. Safavi-Naeini, O. Painter, and F. G. Brandão, Building a Fault-Tolerant Quantum Computer Using Concatenated Cat Codes, *PRX Quantum* **3**, 010329 (2022).
- [28] M. Yuan, Q. Xu, and L. Jiang, Construction of bias-preserving operations for pair-cat code, *arXiv:2208.06913* [quant-ph] (2022).
- [29] Z. Leghtas, S. Touzard, I. M. Pop, A. Kou, B. Vlastakis, A. Petrenko, K. M. Sliwa, A. Narla, S. Shankar, M. J. Hatridge, M. Reagor, L. Frunzio, R. J. Schoelkopf, M. Mirrahimi, and M. H. Devoret, Confining the state of light to a quantum manifold by engineered two-photon loss, *Science* **347**, 853 (2015).
- [30] S. Touzard, A. Grimm, Z. Leghtas, S. O. Mundhada, P. Reinhold, C. Axline, M. Reagor, K. Chou, J. Blumoff, K. M. Sliwa, S. Shankar, L. Frunzio, R. J. Schoelkopf, M. Mirrahimi, and M. H. Devoret, Coherent Oscillations inside a Quantum Manifold Stabilized by Dissipation, *Phys. Rev. X* **8**, 021005 (2018).
- [31] R. Lescanne, M. Villiers, T. Peronnin, A. Sarlette, M. Delbecq, B. Huard, T. Kontos, M. Mirrahimi, and Z. Leghtas, Exponential suppression of bit-flips in a qubit encoded in an oscillator, *Nat. Phys.* **16**, 509 (2020).
- [32] J. M. Gertler, B. Baker, J. Li, S. Shirol, J. Koch, and C. Wang, Protecting a bosonic qubit with autonomous quantum error correction, *Nature* **590**, 243 (2021).
- [33] H. Wang, M. Mariantoni, R. C. Bialczak, M. Lenander, E. Lucero, M. Neeley, A. D. O'Connell, D. Sank, M. Weides, J. Wenner, T. Yamamoto, Y. Yin, J. Zhao, J. M. Martinis, and A. N. Cleland, Deterministic Entanglement of Photons in Two Superconducting Microwave Resonators, *Phys. Rev. Lett.* **106**, 060401 (2011).
- [34] E. A. Wollack, A. Y. Cleland, R. G. Gruenke, Z. Wang, P. Arrangoiz-Arriola, and A. H. Safavi-Naeini, Quantum state preparation and tomography of entangled mechanical resonators, *Nature* **604**, 463 (2022).
- [35] I. L. Chuang, D. W. Leung, and Y. Yamamoto, Bosonic quantum codes for amplitude damping, *Phys. Rev. A* **56**, 1114 (1997).
- [36] M. H. Michael, M. Silveri, R. Brierley, V. V. Albert, J. Salmilehto, L. Jiang, and S. Girvin, New Class of Quantum Error-Correcting Codes for a Bosonic Mode, *Phys. Rev. X* **6**, 031006 (2016).
- [37] B. Royer, S. Singh, and S. Girvin, Encoding Qubits in Multimode Grid States, *PRX Quantum* **3**, 010335 (2022).
- [38] R. Gautier, A. Sarlette, and M. Mirrahimi, Combined Dissipative and Hamiltonian Confinement of Cat Qubits, *PRX Quantum* **3**, 020339 (2022).
- [39] R. E. Slusher, L. W. Hollberg, B. Yurke, J. C. Mertz, and J. F. Valley, Observation of Squeezed States Generated by Four-Wave Mixing in an Optical Cavity, *Phys. Rev. Lett.* **55**, 2409 (1985).
- [40] A. Heidmann, R. J. Horowicz, S. Reynaud, E. Giacobino, C. Fabre, and G. Camy, Observation of Quantum Noise Reduction on Twin Laser Beams, *Phys. Rev. Lett.* **59**, 2555 (1987).
- [41] S. Puri, S. Boutin, and A. Blais, Engineering the quantum states of light in a Kerr-nonlinear resonator by two-photon driving, *npj Quantum Inf.* **3**, 18 (2017).
- [42] H. Putterman, J. Iverson, Q. Xu, L. Jiang, O. Painter, F. G. Brandão, and K. Noh, Stabilizing a Bosonic Qubit Using Colored Dissipation, *Phys. Rev. Lett.* **128**, 110502 (2022).
- [43] S. Rosenblum, P. Reinhold, M. Mirrahimi, L. Jiang, L. Frunzio, and R. J. Schoelkopf, Fault-tolerant detection of a quantum error, *Science* **361**, 266 (2018).
- [44] R. Lescanne, L. Verney, Q. Ficheux, M. H. Devoret, B. Huard, M. Mirrahimi, and Z. Leghtas, Escape of a Driven Quantum Josephson Circuit into Unconfined States, *Phys. Rev. Appl.* **11**, 014030 (2019).
- [45] R. W. Heeres, B. Vlastakis, E. Holland, S. Krastanov, V. V. Albert, L. Frunzio, L. Jiang, and R. J. Schoelkopf, Cavity State Manipulation Using Photon-Number Selective Phase Gates, *Phys. Rev. Lett.* **115**, 137002 (2015).
- [46] K. E. Cahill and R. J. Glauber, Density operators and quasiprobability distributions, *Phys. Rev.* **177**, 1882 (1969).
- [47] P. Milman, A. Auffèves, F. Yamaguchi, M. Brune, J. M. Raimond, and S. Haroche, A proposal to test Bell's inequalities with mesoscopic non-local states in cavity QED, *Eur. Phys. J. D—At., Mol., Opt. Plasma Phys.* **32**, 233 (2005).
- [48] G. Kirchmair, B. Vlastakis, Z. Leghtas, S. E. Nigg, H. Paik, E. Ginossar, M. Mirrahimi, L. Frunzio, S. M. Girvin, and R. J. Schoelkopf, Observation of quantum state collapse and revival due to the single-photon Kerr effect, *Nature* **495**, 205 (2013).
- [49] J. Gambetta, A. Blais, D. I. Schuster, A. Wallraff, L. Frunzio, J. Majer, M. H. Devoret, S. M. Girvin, and R. J. Schoelkopf, Qubit-photon interactions in a cavity: Measurement-induced dephasing and number splitting, *Phys. Rev. A* **74**, 042318 (2006).
- [50] Y. Lin, J. P. Gaebler, F. Reiter, T. R. Tan, R. Bowler, A. S. Sorensen, D. Leibfried, and D. J. Wineland, Dissipative production of a maximally entangled steady state of two quantum bits, *Nature* **504**, 415 (2013).
- [51] S. Shankar, M. Hatridge, Z. Leghtas, K. M. Sliwa, A. Narla, U. Vool, S. M. Girvin, L. Frunzio, M. Mirrahimi, and M. H. Devoret, Autonomously stabilized entanglement between two superconducting quantum bits, *Nature* **504**, 419 (2013).
- [52] M. Kimchi-Schwartz, L. Martin, E. Flurin, C. Aron, M. Kulkarni, H. Tureci, and I. Siddiqi, Stabilizing Entanglement via Symmetry-Selective Bath Engineering in Superconducting Qubits, *Phys. Rev. Lett.* **116**, 240503 (2016).
- [53] Y. Zhang, J. C. Curtis, C. S. Wang, R. J. Schoelkopf, and S. M. Girvin, Drive-induced nonlinearities of cavity modes coupled to a transmon ancilla, *Phys. Rev. A* **105**, 022423 (2022).
- [54] N. Bergeal, F. Schackert, M. Metcalfe, R. Vijay, V. E. Manucharyan, L. Frunzio, D. E. Prober, R. J. Schoelkopf, S. M. Girvin, and M. H. Devoret, Phase-preserving amplification near the quantum limit with a Josephson ring modulator, *Nature* **465**, 64 (2010).
- [55] Y. Y. Gao, B. J. Lester, Y. Zhang, C. Wang, S. Rosenblum, L. Frunzio, L. Jiang, S. M. Girvin, and R. J. Schoelkopf, Programmable Interference between Two Microwave Quantum Memories, *Phys. Rev. X* **8**, 021073 (2018).